Department
Chemie und Pharmazie

FRIEDRICH-ALEXANDER
UNIVERSITÄT
ERLANGEN-NÜRNBERG
NATURWISSENSCHAFTLICHE
FAKULTÄT

Characterization of Interfaces Between Metals and Organic Thin Films by Electron and Ion Spectroscopies

Charakterisierung der Grenzflächen zwischen Metallen und organischen Dünnschichten mittels Elektronen- und Ionenspektroskopie

Der Naturwissenschaftlichen Fakultät der
Friedrich-Alexander Universität Erlangen-Nürnberg

zur Erlangung des Doktorgrades Dr. rer. nat.

vorgelegt von
Martin Schmid
aus Zwiesel

Als Dissertation genehmigt
durch die Naturwissenschaftliche Fakultät
der Friedrich-Alexander Universität Erlangen-Nürnberg

Tag der mündlichen Prüfung: 18. 01. 2012

Vorsitzender der Promotionskomission: Prof. Dr. Rainer Fink

Erstberichterstatter: Prof. Dr. Hans-Peter Steinrück

Zweitberichterstatter: Prof. Dr. Andreas Görling

Für meine Familie

Contents

1 Introduction 1

1.1 Coordination chemistry of tetrapyrroles on Ag(111) and Au(111) surfaces . . . 2

1.2 Chemical reactions at metal/organic interfaces 4

1.2.1 Covalent adsorbate structures on Ag(111) . . 4

1.2.2 The polymer poly(3-hexylthiophene) as substrate for metallic Ca layers 6

1.2.3 Ionic liquids on solid substrates: The solid/liquid interface studied with surface science techniques 7

2 Experimental Methods 9

2.1 Photoelectron Spectroscopy 9

2.1.1 The photoeffect and thermodynamic relations 12

2.1.2 Spin effects in XPS: Spin-orbit splitting and multiplets 15

2.1.3 Quantitative XPS 18

2.1.4 Approximating a Voigt profile 21

2.1.5 Introducing asymmetry 22

2.1.6 Investigating valence levels with UPS 38

2.1.7 Further reading 39

2.2 Low-Energy Electron Diffraction – LEED 40

2.3 Low-Energy Ion Scattering Spectroscopy – LEIS . . 43

3 Results 46

3.1 Coordination chemistry of metallotetrapyrroles on Ag(111) and Au(111) surfaces 46

3.1.1 Cobalt(II) phthalocyanine adsorbed on Ag(111) [P1] 46

3.1.2 Co(II) and Fe(II) tetrapyrroles on Au(111) [P2, P3] 50

3.2 Chemical reactions at the organic/metal interface . . 54

3.2.1 Covalently linked adsorbate structures on Ag(111) [P4, P5] 54
3.2.2 The interface calcium/rr-poly(3-hexylthiophene) [P6] 56
3.2.3 Pd nanoparticles and their interaction with ionic liquids [P7] 60

4 Summary **63**

5 Acknowledgement **69**

6 Bibliography **71**

7 Appendix: [P1] – [P7] **82**

List of Figures

1 2H-Porphyrin and 2H-Phthalocyanine 3
2 The interfacial formation of poly(p-phenylene-terephthalamide) 5
3 The regio regular morphology of the polymer poly(3-hexylthiophene) 6
4 The ionic liquid [EMIM][EtSO$_4$] 8
5 XPS and UPS survey spectra of Au(111) 10
6 Asymmetric Pseudo-Voigt functions 24
7 The finiteness of the integral of an asymmetric Lorentzian curve 26
8 The finiteness of the integral of an asymmetric Gaussian curve 28
9 Auxiliary function for the convergence proof of an asymmetric Gaussian peak 29
10 The finiteness of the integral of an asymmetric Gaussian curve; asymmetry induced by a shifted sigmoidal FWHM-function 31
11 Fit results: Sulphur on Pd(100) 33
12 Fit results: C_2H_2/Pd(100) 35
13 Fit results: Pd 3d signal of Palladium nanoparticles . 37
14 LEIS spectra from the system Ca/Au(111) 44
15 Co 2p core level spectra of cobalt phthalocyanine . . 47
16 Least-squares fit: Co(II) phthalocyanine multilayer . 48
17 LEED patterns: Au(111) and iron phthalocyanine monolayer on Au(111) 51
18 Fe 2p$_{3/2}$ spectra of iron tetrapyrroles on Au(111) . . 52
19 Terephthaloylchloride and p-phenylene dicarbonyl . 54
20 Deposition of Ca onto Au(111) and rr-P3HT 56
21 Ca 2p spectrum of Ca depostited at 130 K and 300 K onto rr-P3HT 58

22 [BMIM][Tf_2N] adsorbed on Pd/Al_2O_3/NiAl(110) . 60
23 Stoichiometry of the ionic liquid [BMIM][Tf_2N] on a Pd based model catalyst 62

List of Tables

1 Fit results S 2p; sulphur on Pd(100) 34
2 Fit results C 1s of C_2H_2/Pd(100) system 36
3 Fit results Pd 3d; Laboratory XPS setup 37
4 Fit results Ca 2p deposited on rr-P3HT at 130K . . . 59

1 Introduction

The surface of a macroscopic object comprises only of an extremely small fraction of the atoms that build up the whole object. However, the interaction of this object with its environment is in many cases determined by the response of this thin, outer layer to the physical or chemical forces associated with the interaction. This is a general concept. The stability of several metals on air is caused by the formation of a protective oxide layer on the surface of the object, i.e., a thin interfacial layer controls a macroscopic property of the object. The same holds true for effects like friction, electrical conductivity, wetability and optical appearance, to name only a few examples.[1] Furthermore it was shown that by choosing a suitable adsorbate, those interfacial properties can be modified in a specific way, for instance to meet requirements within a scientific or industrial application. In recent years it became clear that also organic molecules, and in particular biomolecules, can be utilized for such a purpose. The great variability of organic compounds, in connection with the possibility to synthesize adsorbates particularly tailored to specific applications, gave rise to fields like organic electronics[2–4] or solar energy conversion[5–7] based on organic molecules. In order to obtain a fundamental understanding of the complex inorganic/organic interfaces involved in such applications, it has been a general approach to study relatively simple prototype-like model systems with surface science techniques. A reduction of the complexity should reveal the basic mechanisms. The aim of the present work is to elucidate several aspects of interfaces between metals, like Ag, Au, and Ca and organic matter, as for instance polymers or large, functional biomolecules. Thereby, the focus is set on two different classes of metal/organic interfaces. First, interfaces determined by coordinative ligand interactions and self-assembly of the adsorbate, and second, interfaces determined or even created by a chemical reaction between adsorbate and substrate. The adsorbate/substrate systems were examined under ultra-clean ultra-high vacuum UHV conditions with photoelectron and ion spectroscopies.

1.1 Coordination chemistry of tetrapyrroles on Ag(111) and Au(111) surfaces

Tetrapyrroles, such as porphyrins and phthalocyanines (Figure 1), and their metalated derivatives play a major role in many biological and biochemical processes. The oxygen and carbon dioxide transport in the blood stream of mammals is mediated by iron porphyrins embedded into the heme-protein[8,9] and the photosynthetic process of plants is based on the light absorption by magnesium porphyrin units in chlorophyll,[10–12] to name a few examples. It were the interesting and versatile properties of porphyrins, and in particular their metalated derivatives, that motivated the examination of their electronic structure with photoelectron spectroscopy, starting already in the early 1970s.[13–19] While most of the early work on tetrapyrroles focused on their bulk properties, it were, e.g., Nishimura and co-workers[20], who demonstrated the ex-situ metalation of a thin, well defined interfacial layer of porphyrins. Exposition of a self-assembled monolayer (SAM)[21] of thiol-derivatized 2H-tetraphenylporphyrin (2HTPP) to solutions of various metal salts resulted in the formation of the corresponding metalated derivatives, i.e., in the substitution of the two hydrogen atoms in the central cavity of the porphyrin macrocyle with a metal ion, usually in its +2 state. Similar metalation processes at the solid-liquid interface have been reported for instance by Hanzlikova et al.[22] and Tsukahara and co-workers.[23] It was later shown by Gottfried et al.[24] that the metalation of free base porphyrins and phthalocyanines can be achieved in an ultra-clean ultra-high-vacuum environment (UHV) in a two step process; first, the preparation of a monolayer of the free base porphyrin/phthalocyanine, and second, a physical vapor deposition of the respective metal atoms onto the sample, under certain conditions followed by annealing.[25] This experimental approach opened up the field for the in-situ synthesis and examination of extremely thin films of metallotetrapyrroles that are not stable under regular ambient conditions, like for instance iron(II) tetraphenylporphyrin (FeTPP). The recent scientific interest in the properties of monomolecular films of porphyrins and phthalocyanines on solid substrates stems from the fact that substantial interfacial modifications can be achieved by the adsorption of those molecules; a find-

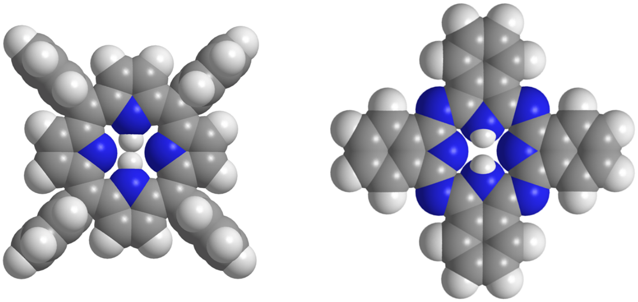

2H-Tetraphenylporphyrin
2HTPP

2H-Phthalocyanine
2HPc

Figure 1. 2H-Tetraphenylporphyrin (2HTPP) and 2H-Phthalocyanine (2HPc).

ing that has been utilized for instance in heterogeneous catalysis,[26,27] molecular electronics,[28,29] or gas sensors[30]. Moreover, it was shown that tetrapyrrole molecules form well ordered, flat lying adsorbate structures on Ag(111) and Au(111) surfaces. The resulting well-defined, prototypical interfaces can be used for a further examination of substrate-adsorbate interactions. Following this approach, it was demonstrated that the interaction between Fe and Co metallo-tetrapyrroles, and an Ag(111) surface can be described by considering the surface as a further, macroscopic ligand to the central metal ion.[31–36] While the metal centers of the free metallotetrapyrroles are fourfold coordinated, a fivefold coordination is achieved in molecules in direct contact to metal substrates. It was further shown that an attachment of nitrogen monoxide (NO) to the remaining sixth coordination site of cobalt(II) tetraphenylporphyrin (CoTPP) molecules on Ag(111) efficiently weakens the coordinative bond between the Co-ions and the Ag(111) substrate;[32] this finding has been interpreted in analogy to the well known trans-effect in coordination chemistry as *surface-trans effect.*[37] The present study aims to further elucidate the coordinative interfacial interactions between metallotetrapyrrole monolayers and Ag(111) or Au(111) substrates.

1.2 Chemical reactions at metal/organic interfaces

While the interfacial properties of tetrapyrrole/metal interfaces are mainly determined by relatively weak coordinative and van der Waals interactions, more severe chemical modifications of adsorbate and/or substrate play a major role at the interfaces discussed in the next sections.

1.2.1 Covalent adsorbate structures on Ag(111)

The well ordered tetrapyrrole adsorbate structures on Ag(111) and Au(111), discussed in the previous paragraph, arise from relatively weak intermolecular interactions; beyond van der Waals interactions, there is no significant covalent coupling between the adsorbed molecules. In a recent study, Grill and co-workers[38] have demonstrated that the halogen-substituted porphyrin compound Br_4TPP can be utilized for the fabrication of well ordered, but covalently interlinked adsorbate structures. After a thermal cleavage of the $C-Br$ bonds, located at the *para*-positions of the four phenyl substituents, the adsorbate molecules interlink with each other via the formation of new $C-C$ bonds between different porphyrin units. The approach of depositing halogen-substituted molecular building blocks to fabricate covalent 2D networks was successfully applied with different combinations of adsorbates and substrates.[39–41] Recently, Schmitz et al.[42] demonstrated the fabrication of chains of poly(*p*-phenylene-terephthalamide) (PPTA, trademark *Kevlar*) on an Ag(111) interface, achieved by the co-adsorption of the precursor molecules terephthaloylchloride (TPC) and *p*-phenylenediamine (PPD). Figure 2 illustrates the corresponding reaction. The resulting polymer chains were self-assembled into well ordered clusters on the Ag(111) interface. This underlines the influence of the two-dimensional environment to the morphological structure of the reaction products. However, it was not clear whether the Ag(111) substrate plays an active role in the formation of the PPTA chains. In solution, the formation of PPTA proceeds via a nucleophilic acyl substitution, resulting in a release of HCl.[42,43] It is not clear if this holds true for the PPTA synthesis on the Ag(111) interface as well. While Schmitz and co-workers so far demonstrated the successful formation of PPTA by means of scanning tunneling microscopy (STM),[42] the present study will further investigate the reaction mechanism and in particular the adsorption behaviour of terephthaloylchloride. This is motivated by the fact that several halogen-substituted molecules are known to adsorb dissociatively on Ag(111).[44,45]

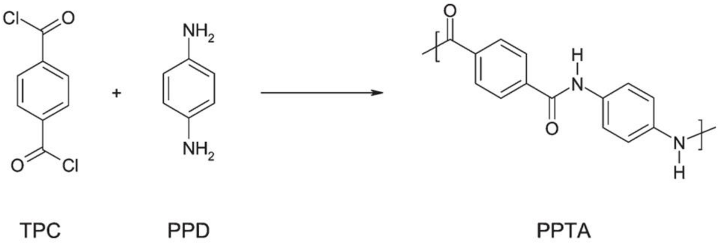

Figure 2. The reaction mechanism for the formation of poly(*p*--phenylene-terephthalamide).

1.2.2 The polymer poly(3-hexylthiophene) as substrate for metallic Ca layers

The formation of interfaces between polymer structures and metals can be achieved as outlined above, where the adsorbate is subject to a polymerization reaction, or alternatively in a reverse approach, by using the organic polymer matrix as a substrate and depositing a metal on top. An example is the interface between metallic calcium and regioregular poly(3-hexylthiophene), abbreviated rr-P3HT (Figure 3); this combination is of great interest since it comprises of a π-conjugated, semiconducting polymer and the low work-function metal calcium. Such metal-semiconductor interfaces are of major importance in organic electronics or optoelectronics, for example in organic light-emitting diodes,[46] field-effect transistors,[47,48] or solar cells[49]. Recently, Zhu and co-workers[51] investigated the properties

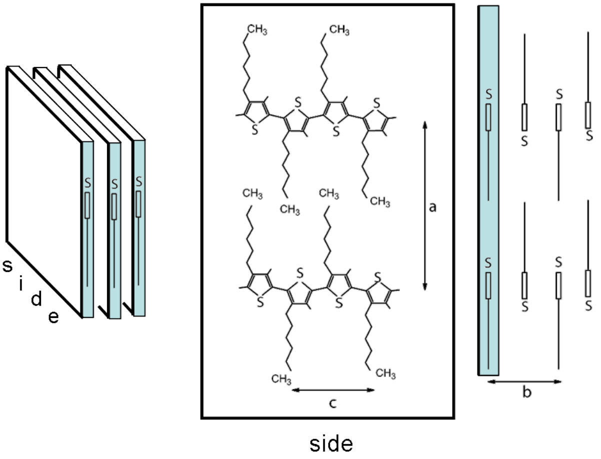

Figure 3. Basic unit of the regioregular polymer poly(3-hexylthiophene), rr-P3HT; modified reprint from Hugger and co-workers.[50] The lattice parameters a, b, and c are as follows: a = 0.168 nm, b = 0.766 nm, and c = 0.77 nm.

of this interface by vapor depositing calcium onto a ≈ 100 nm thick film of rr-P3HT. By employing a variety of surface science techniques it was possible to obtain a comprehensive picture of the interface between Ca metal and the rr-P3HT polymer. A close inspection of the Ca/P3HT interface revealed the presence of a reaction layer where the sulphur atoms within the rr-P3HT matrix react with diffused Ca atoms. The thickness of this diffusion layer was estimated to approximately 3 nm. An improved preparation procedure, resulting in better defined interfaces between Ca and rr-P3HT, i.e., interfaces with a significantly smaller reacted layer, will be addressed in the present work.

1.2.3 Ionic liquids on solid substrates: The solid/liquid interface studied with surface science techniques

A further type of metal/organic interface, which was not discussed up to now, is formed between solids and liquids. Unlike the solid/solid or solid/vacuum interfaces discussed so far, the properties of solid/liquid interfaces are usually not accessible by UHV surface science techniques; the low-pressure environment of UHV experiments ($p < 1 \times 10^{-8}$ mbar) leads to an instantaneous evaporation of liquid (organic) compounds. However, a special class of liquid materials, suitable for UHV experiments, is known as *ionic liquids* (ILs). An ionic liquid is an organic salt, which is in its liquid state at temperatures below 100 °C. Figure 4 illustrates typical cations and anions in ionic liquids. Those compounds have usually vapor pressures below $p < 1 \times 10^{-10}$ mbar, thus furnishing a liquid media that can be stored and examined under UHV conditions. Since ionic liquids are made from easy to synthesize organic compounds, there are potentially $> 1 \times 10^{6}$ different ionic liquids accessible.[52–54] Thus it is feasible to design ionic liquids with respect to given technological or scientific demands. Recent applications of ionic liquids can be found in the field of heterogeneous catalysis, where their application gave rise to novel concepts like SILP[55–57](Supported Ionic Liquid Phase) or SCILL[58] (Solid Catalyst with Ionic Liquid Layer). While in a SILP approach the ionic liquid acts as a solvent for a catalytically active compound, a SCILL catalyst comprises of a solid heterogeneous catalyst, covered with an ionic liquid with particularly designed properties. In both cases, the ionic liquid may act as a semipermeable membrane or solvent for educts or products of the catalytic process.

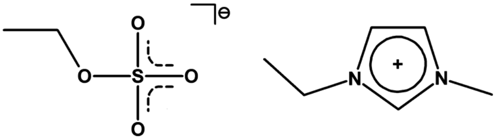

1-ethyl-3-methylimidazolium
ethylsulfate,
[EMIM][EtSO$_4$]

Figure 4. The ionic liquid [EMIM][EtSO$_4$]; the first ionic liquids have been synthesized already in 1914 by Walden.[59]

Since it was recently demonstrated that thin and ultra-clean films of ionic liquids can be prepared by physical vapor deposition (PVD),[60] the examination of ionic liquid interfaces is possible with conventional surface science techniques, as for instance photoelectron spectroscopy.[60–63] This offers an experimental route to examine electronic structures and chemical processes at the solid/liquid interface in typical SCILL or SILP type experiments.[64] The present study will focus on the interfacial interactions between the room temperature ionic liquid 1-butyl-3-methylimidazolium bis(trifluoromethylsulfonyl)imide, [BMIM][Tf$_2$N], and the model catalyst surface Pd/Al$_2$O$_3$/NiAl(110). Briefly, this Pd-nanoparticle based model catalyst has been extensively utilized to approximate catalytic processes at a level of complexity still resolvable by conventional surface science techniques.[65–68] The active sites of this model catalyst, the Pd-nanoparticles, consist of approximately 3000 atoms (600 surface atoms), and adopt a cuboctahedral shape where the major facets (top-facet and side-facets) show a (111) orientation. A (100) orientation of a part of the side facets can be observed, nevertheless the majority of the sites ($\approx$ 80%) exhibit (111) orientation. Typically $\approx$ 20% of the aluminium oxide substrate is covered with those particles.[64–68]

2 Experimental Methods

In this section we will briefly review the most fundamental aspects of the experimental methods which have been utilized in this thesis. We will concentrate in particular on those aspects that are essential to the interpretation of experimental results. The reader who is interested in further details is referred to the literature listed at the end of this chapter.

2.1 Photoelectron Spectroscopy

Photoelectron spectroscopy measures the energy distribution of electrons in a sample. Beyond qualitative information as, e.g., the existence of valence states, it is possible to obtain information on band structures in solids or oxidation states in molecules. The method is based on the photoelectric effect, i.e., the phenomenon that irradiation of a sample with photons of a sufficient energy (typically $h\nu > 5$ eV) results in an emission of electrons from the sample. The kinetic energy of an individual photoelectron is determined by the photon energy $h\nu$ and its binding energy prior to ionization by the following equation:[a]

$$E_{kin} = h\nu - E_{bind}$$

Hence, by measuring the distribution of the kinetic energy of an ensemble of photoelectrons one can deduce the binding energy distribution within the sample. Depending on the energy range of the utilized photons it is common practice to distinguish between UPS (UV Photoelectron Spectroscopy) and XPS (X-ray Photoelectron Spectroscopy, or synonymous ESCA - Electron Spectroscopy for Chemical Analysis). Common photon energies employed for UPS are 21.22 eV (HeI discharge) or 40.8 eV (HeII discharge), and for XPS 1253.6 eV (Mg Kα line) or 1486.6 eV (Al Kα line).

---

[a] Here we define the binding energy as the amount of energy necessary to remove an electron completely from the sample. However, in applications it is more practicable to define the binding energy relative to the Fermi edge of the corresponding solid. Both definitions differ by the work function ϕ, i.e., the energy required to move an electron from the Fermi edge into the vacuum.

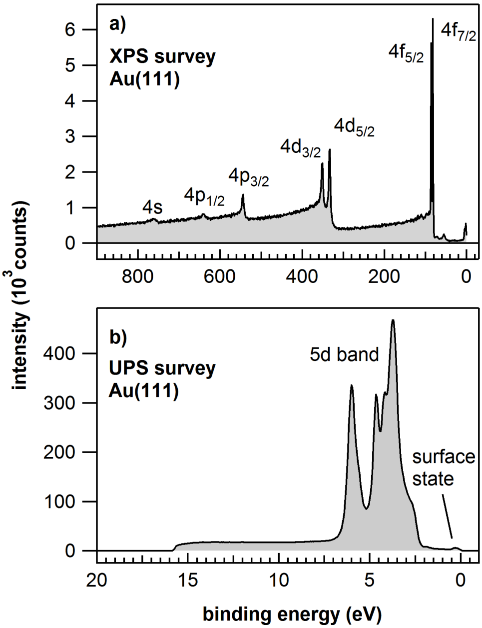

Figure 5. Survey spectra of Au(111) acquired with (a) X-ray (1486.6 eV) and (b) UV (21.2 eV) radiation. The intensity axis shows typical intensities in XPS and UPS experiments; the UPS spectrum of the Au 5d band clearly demonstrates the higher resolution of UPS in a more narrow spectral range close to the Fermi edge. Moreover, UPS resolves the Au(111) Shockley type surface state.[69] With UPS, the work function of the sample can be determined as the difference between the photon energy (21.2 eV) and the spectral width (energy range of the gray shaded region in frame b) of 15.8 eV); see text for details.

An example for a typical X-ray photoelectron spectrum is shown in Figure 5 a). The core level spectrum is comprised of relatively few, narrow lines, each representing a certain electronic state. The intensity of such a line is directly proportional to the abundance of the corresponding binding energy level within the sample, and thus to the abundance of the corresponding atom. Each atomic species has an individual characteristic photoelectron pattern, as indicated in Figure 5 b) for the case of gold. We will come back to the nomenclature of the photoelectron lines in Chapter 2.1.2. In a compound material, e.g., a metal alloy, the photoelectron spectrum is the sum of the photoelectron patterns from each of the individual components. The relative intensity of those different photoelectron patterns, corrected for individual atomic sensitivity factors, directly reflects the stoichiometric composition of the sample. Aside from the possibility to quantify the atomic composition of a sample, changes in the chemical state of a given atom usually shift the binding energy positions of its photoelectron lines in the range of several electron volts. Thus, the method can be used not only to identify and quantify different atoms, but also to distinguish between atoms of the same element in different chemical environments. As depicted in Figure 5 a), the discrete line pattern is superimposed to a background signal, which mainly originates from inelastic interactions of photoelectrons during passing through the sample material. These interactions lower the kinetic energy of the photoelectrons, therefore the respective structures appear at higher binding energies. It is common practice to subtract background features by algorithms proposed by Shirley[70] or, more rarely, Tougaard.[71] It is an essential feature of photoelectron spectroscopy that only electrons from a relatively thin surface layer of the sample contribute significantly to the signal. The flux of photoelectrons excited inside the bulk material of the sample is attenuated according to Lambert-Beer's law by the surrounding sample material. Therefore, only photoelectrons which were excited in the first few nanometers below the surface can leave the sample and enter the spectrometer, rendering photoelectron spectroscopy an extremely surface sensitive method. The *inelastic mean free path* λ, i.e., the average distance that an electron can travel through a solid without suffering energy loss, is generally a function of its kinetic energy. We will discuss this quantity in more detail in a later chapter, but note that it has typically values in the range of some 1×10^{-9} m. In contrast to XPS, UV photoelectron spectroscopy cannot be used to acquire quantitative information on the chemical composition,[72] since the direct proportionality between the signal intensities and the abundance of the corresponding electronic level does not hold here; nevertheless, qualitative information, e.g., on the existence of valence states can be derived with UPS with a higher energy resolution compared to a common XPS setup.[72] A UPS survey spectrum of a clean Au(111) surface is displayed in Figure 5 b). We will discuss some selected facets of photoelectron spectroscopy, in particular those in direct relation to the results presented in this work, in the following sections.

2.1.1 The photoeffect and thermodynamic relations

This paragraph is dedicated to a justification of the simple relation between the kinetic energy of photoelectrons, the energy of the impinging photons, and the binding energy of the electrons within the sample. The simple relation (1) between those quantities is the fundamental equation of photoelectron spectroscopy. Instead of discussing the quantum mechanical treatment of the photoeffect, which can be found for instance in the textbook of Hüfner,[72] we will follow the historical development of the theory. Based on the classical description of the energy density of the radiation field of a black body, we will follow the argumentation of Einstein.[73] By employing fundamental thermodynamic principles, we will find evidence that the energy of an electromagnetic radiation field appears to be evenly distributed to an ensemble of smallest, discrete quanta, each of the size $h\nu$. Here, h is Planck's constant and ν is the frequency of the radiation. By referring to such a quantum of radiation energy as a *photon*, one can directly identify the intensity of a radiation field with the number of photons and explain the experimental result that a higher intensity of the radiation field does not, as classical electrodynamics demands, lead to an increased kinetic energy, but to a higher number of photoelectrons with a kinetic energy of:

$$E_{kin} = h\nu - E_{bind} \tag{1}$$

The starting point of our calculation is Wien's approximation (equation (2)), which gives the energy density of the radiation field of a black body in the limit of high frequencies.

$$\rho = \alpha \nu^3 e^{-\frac{h\nu}{kT}} \tag{2}$$

Or, after rearranging

$$\frac{1}{T} = -\frac{k}{h\nu} \ln\left(\frac{\rho}{\alpha\nu^3}\right) \tag{3}$$

The next step is the definition of an auxiliary function φ, related to the entropy (according to Wien)[73,74]

$$S = V \cdot \int_0^\infty \varphi_{(\rho,\nu)}\, d\nu$$

which represents the entropy of the radiation field per frequency and volume. For black body radiation Einstein deduces:[73]

$$\frac{\partial\varphi}{\partial\rho} = \frac{1}{T}$$

A comparison with equation (3) results in a differential equation:

$$\frac{\partial\varphi}{\partial\rho} = -\frac{k}{h\nu} \ln\left(\frac{\rho}{\alpha\nu^3}\right)$$

Here, simple integration [b] results in an analytical expression for φ:

$$\varphi_{(\rho,\nu)} = -\rho\, \frac{k}{h\nu} \left[\ln\left(\frac{\rho}{\alpha\nu^3}\right) - 1\right]$$

Considering the entropy of quasi monochromatic radiation with a frequency between ν and $d\nu$ within a volume V, we find

$$dS_{(\nu,\nu+d\nu)} = V\varphi_{(\rho,\nu)}\, d\nu = -V\rho\, \frac{k}{h\nu} \left[\ln\left(\frac{\rho}{\alpha\nu^3}\right) - 1\right] d\nu$$

Substituting the total energy of this radiation, $dE = \rho V\, d\nu$, we obtain:

$$dS_{(\nu,\nu+d\nu)} = -dE\, \frac{k}{h\nu} \left[\ln\left(\frac{dE}{V\alpha\nu^3 d\nu}\right) - 1\right] \tag{4}$$

This is an expression for the entropy of the radiation of energy dE, contained in a volume V. In a final step, we discuss the change of the entropy associated with a variation of the volume. Considering an entropy of dS_0 related to a volume V_0 and calculating the entropy difference, we obtain:

---

[b] $\int \ln(x)\, dx = x\ln(x) - x$

$$dS - dS_0 = dE\,\frac{k}{h\nu}\ln\left(\frac{V}{V_0}\right) \qquad \text{or} \qquad dS - dS_0 = k\ln\left(\frac{V}{V_0}\right)^{dE/h\nu} \tag{5}$$

For the sake of clarity, we will follow the original work[73] and simplify the equations by writing simply S instead of $dS_{(\nu,\nu+d\nu)}$ of the quasi-monochromatic radiation. Analogue, we will express the energy of the quasi-monochromatic radiation with E instead of $dE_{(\nu,\nu+d\nu)}$ Thereby, Equation (5) changes into:

$$S - S_0 = k\ln\left(\frac{V}{V_0}\right)^{E/h\nu} \tag{6}$$

Considering an ideal gas of N particles contained in a volume V_0, the statistical probability of a spontaneous assembly of all particles in a sub-volume V is given by

$$P = \left(\frac{V}{V_0}\right)^{N}$$

The change in entropy by such a process is:

$$S - S_0 = k\ln\left(\frac{V}{V_0}\right)^{N} \tag{7}$$

Equations (6) and (7) are identical if setting $N = E/h\nu$. The entropy of a quasi-monochromatic radiation field with the energy E depends on the volume in a similar fashion as the entropy of an ideal gas with the total energy E. This result is only valid as long as the total energy of the radiation field is infinitesimal small and the radiation frequency is large enough to guarantee the validity of Equation (2). Thus, Equation (6) only holds true as long as a high frequency radiation field has a small total energy density, like for instance X-ray radiation with a small total energy contained in a large volume.

The finding that the entropy of the radiation field is well described if one assumes that its total energy is evenly distributed to $N = E/h\nu$ energy quanta, led Einstein to his conclusion regarding the photoeffect. Equation (1) follows directly from this assumption.

While those arguments help to rationalize the energy quantification of a radiation field and Equation (1), they fail to explain more advanced features of the photoeffect, such as the quenching of certain photoelectron lines by symmetry selection rules during experiments with polarized photons. Those effects can be understood only by applying the more advanced quantum mechanical description of the interaction between radiation and matter. The interested reader is referred to the literature at the end of this chapter.

2.1.2 Spin effects in XPS: Spin-orbit splitting and multiplets

In this section, we will discuss effects that lead to the generation of multiple lines in XPS core level spectra, due to the presence of spins, or generally angular momenta.

As a first effect, we will consider the spin-orbit splitting which is present in the photoelectron lines from non-s orbitals. This effect is responsible for the splitting of the atomic p, d, and f states into doublets and is clearly visible in the XPS spectrum in Figure 5 b). This phenomenon arises because the angular momentum of the electron, orbiting the atomic nucleus, couples with the electron spin. Depending on the relative orientation of both magnetic moments, parallel or anti-parallel, the signal appears at a reduced or higher binding energy. This explains, for instance, the splitting of the Au $4d$ level ($l = 2$) into $4d_{3/2}$ and $4d_{5/2}$ sub-levels, as shown in Figure 5. The total angular momentum j of each doublet state, as indicated by the subscripts $3/2$ or $5/2$, simply results from the corresponding angular momentum l and the electron spin $s = 1/2$ according to $j = l - 1/2$ and $j = l + 1/2$.[75] The magnitude of the corresponding doublet splitting on the binding energy scale is proportional to $1/\langle r^3 \rangle$, where $\langle r \rangle$ represents the average radius of the corresponding orbital.[75] Thus, orbitals with different spatial dimensions will show a different spin-orbit splitting. As Figure 5 a) illustrates for the case of gold atoms, the spin-orbit separation is largest for p electrons and smallest for f electrons. This reflects the fact that $\langle r \rangle_{p\ electrons} < \langle r \rangle_{d\ electrons} < \langle r \rangle_{f\ electrons}$. The intensity ratio between the individual doublet states is given by their degeneracy. Accordingly, the $2p_{1/2}$ and $2p_{3/2}$ sub-levels will show an intensity ratio of $2 : 4$, since the $2p_{1/2}$ level is twofold de-generated, while the $2p_{3/2}$ is of fourfold degeneracy.[75]

Generally, both peaks of a doublet, may it emerge from a *p*, *d*, or *f* state, differ only in their relative intensity, but are of virtually identical shape. Exceptions from this general behaviour can be observed in particular in the core level spectra of transition metals.[76] There, a broadening of the $2p_{1/2}$ state relative to the $2p_{3/2}$ state is evident. Since the natural line width of a photoelectron signal is determined by the lifetime of the respective core-hole,[72] it follows that the lifetime of the $2p_{1/2}$ core hole has to be smaller than the lifetime of the corresponding $2p_{3/2}$ state. This finding can be explained by the fact that the $2p_{1/2}$ core hole has an additional decay channel, i.e., the decay via a $L_2L_3M_{4,5}$ Coster-Kronig Auger electron process, resulting in a higher decay probability and accordingly a shorter lifetime.[77,78] During this process, an electron originating from the $2p_{3/2}$ level fills up the $2p_{1/2}$ core hole; the energy difference between those two states is released via an Auger-Electron. The resulting broadening of transition metal $2p_{1/2}$ states compared to the corresponding $2p_{3/2}$ lines is well described in the literature.[77,78]

A further effect that complicates in particular the analysis of transition metal core level spectra is the appearance of multiplet effects due to the presence of further, unpaired spins, for instance in the *d*-subshell of transition metal complexes.[79,80] The coupling between unpaired electrons in the *d*-shell with the photoion core-hole gives rise to several energetically different final states. This phenomenon can be observed in all core-levels, including *s* orbitals.[79] The detailed mechanism of this coupling, and subsequently the resulting peak pattern has been subject to several theoretical approaches. In the following section we will briefly review this topic, since it is essential for the interpretation of the photoelectron spectra acquired from metallotetrapyrrole samples.

Multiplet effects were detected in the *s* orbitals of paramagnetic molecules, such as O_2 or NO,[81] as well as in transition metal compounds[79,82,83]. This phenomenon has been interpreted as a final state effect. Since the process of photoionization obeys energy conservation, the different results of the coupling process, i.e., the different magnetic states of the photoion, are reflected by different corresponding kinetic energies of the detected photoelectron. The magnitude of this splitting is enhanced by correlation effects if the s-core hole and the unpaired electrons belong to the same atomic shell, as for instance in the case of a $3s$ core-hole in a $3d$ transition metal complex.[84] The interpretation of a corresponding multiplet splitting in p or d levels proved to be more complex; in a first approximation one could describe the resulting lines as the result of a *core-spin + core-orbit + d-spin + d-orbit* coupling. In particular Gupta and Sen[85,86] developed a theory that additionally takes an influence of excited states of the d-electrons into account, resulting in a relatively complex multiplet pattern in the $2p$ levels of $3d$ transition metal complexes. Nevertheless, their results were applied successfully in several studies.[80,87–89] Alternatively to the Hartree-Fock calculations of Gupta and Sen, a relatively simple angular momentum coupling scheme was successfully applied, in particular to cobalt high-spin (S=3/2) and cobalt low-spin (S=1/2) compounds.[15,16,90–92] This coupling scheme is based on theoretical considerations of Nefedov.[93] Essentially, it neglects any angular momentum of the d-electrons,[94] while coupling the $2p_{1/2}$ and $2p_{3/2}$ core hole states exclusively with the resulting spin of the d-electrons. To give a short example, an $S = 1$ spin state of the d-subshell will result in $J = 5/2, 3/2$, and $1/2$ states, originating from the $2p_{3/2}$ state in the photoion, and a doublet of $J = 3/2, 1/2$ states, arising from the $2p_{1/2}$ core-hole.[15,92]

Since the state of the d-electrons strongly affects the 2p spectra, the spin-orbit separation – usually considered as the constant distance between the maxima of the $2p_{3/2}$ and $2p_{1/2}$ peaks – is not well defined any more; there is a variety of different multiplet states that emerge from the $2p_{3/2}$ and $2p_{1/2}$ levels and it is not unambiguously clear which to take to measure the spin-orbit splitting. However, it is common practice to measure the distance between the most intense lines within each multiplet to define the spin-orbit separation. The influence of the d-electrons to the spin-orbit separation was closely examined for instance for various cobalt compounds. Co(II) high-spin compounds generally show an apparent spin-orbit separation of ≈ 16 eV, while diamagnetic Co(0) or Co(III) complexes show a value of only ≈ 15 eV.[15,90,91] For a cobalt atom in a Co(II) (S=1/2) low-spin state, usually a spin-orbit separation of ≈ 15.5 eV is found.[92]

Further specific properties of the core level spectra of paramagnetic transition metal compounds have to be mentioned at this point. It is an established experimental fact that the spin state - at least of cobalt compounds - has a direct influence on the intensity of satellite lines in the corresponding $2p$ region.[15,16,90–92] While Co (II) (S=3/2) compounds show an intense satellite structure, no satellites are observed in the spectra of diamagnetic Co(0) or Co(III).[15,90–92] Co(II) (S=1/2) low-spin compounds, such as cobalt(II) phthalocyanine, which is discussed in more detail in the experimental part, show an intermediate behavior by exhibiting an appreciable, but not dominant satellite structure.[16,92] In conclusion, it can be inferred that each configuration of the d-electrons of cobalt compounds has a distinct spectral fingerprint in the core levels.

2.1.3 Quantitative XPS

As mentioned in the preceding chapter, XP spectra contain information originating nearly exclusively from a thin surface layer with a thickness of several nanometers. In the following section we will elaborate this statement in more detail. The flux of electrons travelling through a solid is exponentially attenuated according the law of Lambert-Beer; the longer the travelled distance x, the lower the residual electron flux $I(x)$.

$$I_{(x)} = I_0 \ \exp\left(-\frac{x}{\lambda}\right)$$

Therefore, only electrons that have travelled a relatively short distance through the sample material, until they have reached and left the surface, contribute significantly to photoelectron signals. The quantity λ is commonly referred to as *attenuation length* or *electron inelastic mean free path*, and is in general a function of the kinetic energy of the electrons. It gives the distance after which an initial electron flux is reduced by a factor of $1/e \approx 0.37$. The other electrons lost kinetic energy or were absorbed during their passage through the sample. These electrons contribute significantly to the background signal of photoelectron spectra. In this study, we use an empirical expression for the dependency of λ on the kinetic energy E according to $\lambda = 0.3\,E^{0.64}$; this expression is only valid for the typical kinetic energies of photoelectrons as observed in XPS measurements.[95] It appears noteworthy that the mean free path of electrons that pass through a solid, shows only a minor dependency to the particular composition of the solid material. A plot of the mean free path as a function of the kinetic energy of the electrons is often referred to as *universal curve*, since it is remarkably independent from any material properties.[96,97] The smallest mean free path, i.e., the highest interaction probability of the electrons with the surrounding material occurs at an energy of ≈ 50 eV. At higher energies, the mean free path increases with increasing energy. The relation for λ - as given above - is thus only an approximation to the *universal curve* in the region of kinetic energies typical for XPS measurements. The depth from which 95% of the detected photoelectrons of a given photoelectron peak emerge is commonly referred to as *information depth*. It equals approximately 3 times the attenuation length.

If photoelectrons, excited at a depth d inside the bulk material, travel towards the surface under an angle $\vartheta \neq 0$, i.e., not on a trajectory parallel to the surface normal, their route through the sample will be of the length $d/\cos(\vartheta)$, resulting in a stronger attenuation of the signal. The following equation describes the influence of the detection angle ϑ to Lambert-Beer's law.

$$I_{(d)} = I_0 \ \exp\left(-\frac{d}{\lambda\ \cos\vartheta}\right)$$

This result allows to vary the effective information depth simply by rotating the sample relative to the spectrometer, and thus detecting only photoelectrons that travelled through the sample under an angle $\vartheta \geq 0$. Accordingly, the depth λ after which the initial flux is reduced to a fraction of $1/e \approx 0.37$ decreases to a value of $\lambda\,\cos\vartheta$, resulting in a higher surface sensitivity of the method. Rotating a sample during XPS measurements furthermore furnishes a method to distinguish surfaces that are built up from subsequent layers of different chemical compounds from surfaces that consist of a random mixture (as e.g. alloys). The latter case shows no variation of the relative intensities of the different elements with the detection angle.

Assuming a layer by layer growth, the intensity of photoelectrons originating from an overlayer of a thickness d, e.g., organic molecules on a metal substrate, can be calculated according to

$$I^{ad}_{(d)} = I^{ad}_{\infty} \left(1 - \exp\left(-\frac{d}{\lambda_{ad}\, \cos\vartheta}\right)\right)$$

In a real experiment the quantity I^{ad} would correspond for instance to the intensity of the C 1s line, or any other intense photoelectron line originating exclusively from the adsorbate. In this equation, I^{ad}_{∞} represents the intensity measured if the layer thickness is allowed to increase to infinity, thus the highest possible count rate. Considering the attenuation of a substrate peak (e.g., the Au4f$_{5/2}$ line with pristine intensity I^{sub}_{∞}) due to the presence of an adsorbate layer of the thickness d, one finds

$$I^{sub}_{(d)} = I^{sub}_{\infty} \exp\left(-\frac{d}{\lambda_{ad}\, \cos\vartheta}\right)$$

Accordingly, the thickness of an adsorbate layer can be calculated from the ratio of the measured intensities of the substrate and adsorbate,[98] $I^{ad}_{(d)}/I^{sub}_{(d)}$, by solving the transcendental equation

$$\frac{I^{ad}_{(d)}}{I^{sub}_{(d)}} = \frac{I^{ad}_{\infty}}{I^{sub}_{\infty}} \frac{\left(1 - \exp\left(-\frac{d}{\lambda_{ad}\, \cos\vartheta}\right)\right)}{\exp\left(-\frac{d}{\lambda_{sub}\, \cos\vartheta}\right)} \approx \frac{\sigma^{ad}}{\sigma^{sub}} \frac{\left(1 - \exp\left(-\frac{d}{\lambda_{ad}\, \cos\vartheta}\right)\right)}{\exp\left(-\frac{d}{\lambda_{sub}\, \cos\vartheta}\right)}$$

The factors σ^{ad} and σ^{sub} represent the *photoionization sensitivity factors* of the photoelectron lines of adsorbate and substrate, respectively. Numerical values for different elements are tabulated in the literature.[99,100] A correct application of the latter equation requires that the spectrometer is operated at identical settings during the acquisition of the substrate and adsorbate spectra.

We have seen in the preceding paragraph, how the intensity of a spectral line can be used to quantify the interfacial composition of a sample, as for instance by calculating the thickness of an adsorbate layer. In many cases the required extraction of a line intensity is complicated by an overlap of several different peaks. In such a situation, only a numerical deconvolution of the signal by a least-squares fit allows further interpretations. While, in a first-order approximation, each photoelectron peak can be modeled as a Gaussian curve, accurate results require the application of peak functions with certain specific properties. The next chapter is dedicated to this issue.

2.1.4 Approximating a Voigt profile

We have seen in the previous chapter that the intensity of a photoelectron line can be used to quantify the amount of the corresponding element on a sample. A reliable measure for the intensity is the area below a photoelectron line. The measurement of this quantity is commonly achieved by a least-squares fit with a suitable peak profile. Such profiles are for instance Doniach-Sunjic curves[72,101] or, in particular in this work, Voigt profiles.[102–104] A Voigt profile is the result of the convolution of a Lorentzian profile with a Gaussian curve. In XPS, the Lorentzian curve represents the actual energy distribution of photoelectrons, originating from a distinct atomic level, as they leave the sample. The spectral width of this line is inversely proportional to the lifetime of the corresponding core-hole in the photoion, a result that follows from the quantum mechanical uncertainty principle between time and energy.[77,78,102] The subsequent imaging of the photoelectrons by the spectrometer results in a distinct perturbation of the initial shape of the spectral line. This perturbation can be described by a convolution with a Gaussian curve. In numerical applications, however, it is an established procedure to approximate the real convolution with a numerically less costly algorithm. Accordingly, it is a widespread practice to approximate the convolution between Gaussian and Lorentzian profiles by the calculation of a sum of Gaussian and Lorentzian curves according to equation (8); m represents a weighting factor with possible values between 0 and 1. Such a weighted sum is commonly referred to as Pseudo-Voigt curve.[105,106]

$$Gauss \otimes Lorentz \approx (1-m)\,Gauss + m\,Lorentz \tag{8}$$

Although the shape of Gaussian and Lorentzian curves can be considered as common knowledge, some modifications, which are often applied in the context of photoelectron spectroscopy, have to be mentioned. In an XPS least-squares fit procedure it is favorable to have the peak area A as a direct coefficient, rather than the amplitude h. This can be achieved due to the finite area of Gauss as well as Lorentz curves. In the following sections we will write x instead of $E - E_0$ for the sake of simplicity; E represents the binding energy scale of XPS spectra, and E_0 the binding energy of a distinct peak. The areas of the Gauss and Lorentz curves are given by

$$\begin{aligned} A_g = & \int_{-\infty}^{\infty} Gauss = & \int_{-\infty}^{\infty} h_g \, e^{-a^2 x^2} \, dx = h_g \, \frac{\sqrt{\pi}}{a} \\ A_l = & \int_{-\infty}^{\infty} Lorentz = & \int_{-\infty}^{\infty} h_l \, \frac{1}{b^2 + x^2} \, dx = h_l \, \frac{1}{b} \arctan\left(\frac{x}{b}\right)\Big|_{-\infty}^{\infty} = h_l \, \frac{\pi}{b} \end{aligned}$$

or in terms of the full width at half maximum (FWHM) $\omega_g = \sqrt{4 \ln 2}/a$ and $\omega_l = b/2$

$$\begin{aligned} A_g = & \quad h_g \, \omega_g \sqrt{\frac{\pi}{4 \ln 2}} \\ A_l = & \quad 2 h_l \, \frac{\pi}{\omega_l} \end{aligned}$$

This analysis allows to substitute h_g and h_l as functions of area and FWHM.

$$\begin{aligned} h_g = \sqrt{\frac{4 \ln 2}{\pi}} \, A_g/\omega_g \quad & \Rightarrow \quad Gauss = \sqrt{\frac{4 \ln 2}{\pi}} \, \frac{A_g}{\omega_g} \, e^{-4 \ln 2 (\frac{x}{\omega_g})^2} \\ h_l = \frac{1}{2\pi} (A_l \, \omega_l) \quad & \Rightarrow \quad Lorentz = \frac{A_l}{2\pi} \, \frac{\omega_l}{(\omega_l/2)^2 + x^2} = \frac{2 A_l}{\pi} \, \frac{\omega_l}{\omega_l^2 + 4 x^2} \end{aligned}$$

2.1.5 Introducing asymmetry

General considerations The signal background of core level spectra is, as mentioned above, the result of energy-loss processes of photoelectrons. Thus, those electrons have a lower kinetic energy and appear accordingly at a higher binding energy. The situation can be complicated if the background shows an irregular shape due to complex energy loss mechanisms, and in particular if those loss-structures overlap with the main peak. Such a situation is frequently observed in the presence of plasmon excitations, i.e., collective oscillations of the sample electrons.[107] Further discrete loss structures are *shake up* and *shake off* satellites, where another electron of the photoion is excited to an initially unoccupied state (shake up), or is even removed from the photoion (shake off - leads to a twofold ionization). Further loss structures, typical for organic molecules are vibrational excitations of the photoion. There, according to the Frank-Condon principle, the exciting photon transfers energy not only to the photoelectron, but also to a molecular vibration.[102,108,109] A situation which is frequently found, specifically in spectra from metallic samples, is a distorted peak shape due to a screening of the photoion core-hole by conduction electrons, and the creation of an electron-hole pair. This loss mechanism usually creates a distinct, asymmetric tail in the range from 0 to 5 eV above the main line.[104] A possible way to introduce such an asymmetry in Pseudo-Voigt functions[105] is the redefinition of the FWHM ω according to $\omega_g = \omega_l = \omega(x)$. If this method is chosen, one has to be aware of several consequences:

(i) FWHM related parameters that enter the fit represent not necessarily the *actual FWHM* of the resulting curve.

(ii) The simple relation between peak area and amplitude, as deduced in the previous chapter, is no longer valid; the area-parameter that enters the fit is not the real area of the peak.

(iii) Depending on the detailed function $\omega(x)$, it is possible that the resulting curve has no finite area; in this case a suitable cut-off criterion for integration has to be chosen.

It follows from the first two points that the actual width and area of the resulting peak have to be measured on the resulting curve; in general, there is no simple, analytical relation between the corresponding fit parameters and the actual values. Furthermore, it is favourable if the function $\omega(x)$ would result in a Pseudo-Voigt curve with a finite and well defined area. In that case no arbitrary cutoff criterion has to be chosen. Recently Stancik and co-workers[110] suggested a sigmoidal variation of $\omega(x)$, according to the equation

$$\omega_{(x)} = \frac{2\,\omega_0}{1+\exp(-ax)} \tag{9}$$

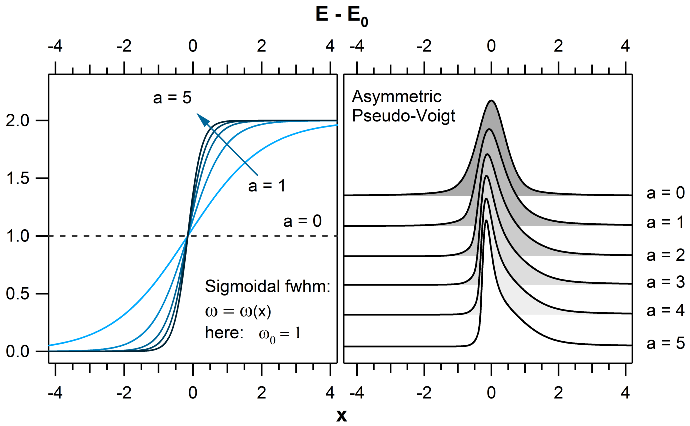

Figure 6. Several asymmetric Pseudo-Voigt functions; the parameter *a* controls the degree of asymmetry.

In this equation, ω_0 represents the FWHM of the corresponding symmetric Pseudo-Voigt peak, while the parameter a determines the degree of asymmetry. In the case of $a = 0$, the resulting curve is simply a symmetric Pseudo-Voigt profile with a FWHM of ω_0. Figure 6 illustrates the resulting curves for several choices of a. The asymmetry parameter a is constrained to positive values only. Although this function was proposed in the context of vibrational spectroscopy, we will see in the following chapters that, after a modification, it furnishes a peak profile usable for XP spectra as well.

Unique profile areas A significant drawback to several asymmetric peak shapes, as for instance, Doniach-Sunjic profiles,[101,104] is the fact that the area below the curve is not well defined. In contrast to the symmetric Gauss and Lorentz functions, where an integration from $-\infty$ to ∞ results in an unique and well defined area, a similar integration of asymmetric profiles yields possibly an infinite area.[72] There, to obtain a finite area, one has to decide for an arbitrary integration range. Hence it is difficult, if not impossible in most cases, to compare different peak areas in an unambiguous way, since it is not possible to decide for an unique, physically justified integration range. The asymmetric Pseudo-Voigt function, as defined above, does not share this disadvantage. Similar to the symmetric Gauss and Lorentz functions, it has a unique profile area. We will prove this statement in the following section. To do so, we will prove the convergence of the integral of the Gauss and Lorentz contributions in the peak separately. The sum of two profiles, each with a convergent integral, is again a profile with a convergent integral.

Since it is difficult to obtain an antiderivative of asymmetric Pseudo-Voigt profiles and deduce the integral directly, we will utilize the following

Theorem 1 *The integral of a curve* $f(x) \geq 0$ *on a given interval is finite, if one can find a different curve* $G(x)$*, with* $G(x) \geq f(x)$ *and* $\int G(x)\,dx = \mathit{finite}$*. We will refer to such a curve as a majorant. If we can show the existence of a majorant in a given interval, we have shown the finiteness of the integral over* $f(x)$ *over that interval.*

We are now in a position to prove the important finiteness of the integral.

Lorentz Let $f(x)$ be an asymmetric Lorentzian curve, where the asymmetry is specified by the parameters ω_0 and a according to Equation (9). The relation $f(x) \geq 0$ is true for all possible x. To obtain a majorant for the Lorentz curve, we will choose a symmetric Lorentzian curve with a width of $4\,\omega_0$. This choice is indicated in Figure 7. We will now deduce the intervals where $f(x) < G(x)$, i.e., the coordinates of the intersection points between $f(x)$ and $G(x)$. On this interval the relation $\int f(x)dx \leq \int G(x)dx$ holds true; since it is known that the integral over $G(x)$ is finite there, one can conclude then that the integral over $f(x)$ is finite on that interval as well. To work out the intersection points we set:

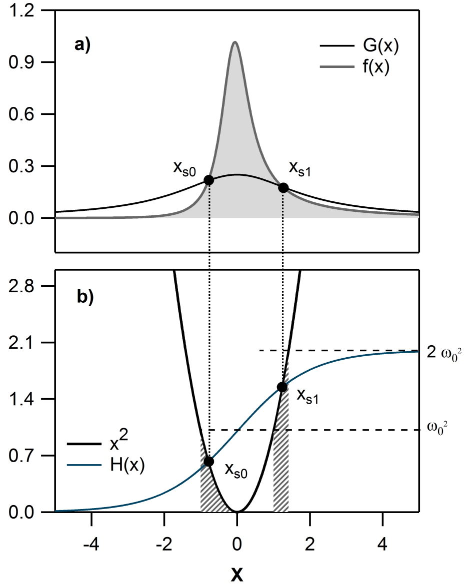

Figure 7. Determination of the intersection points between the asymmetric Lorentz profile, $f(x)$ and its majorant curve $G(x)$. The dashed regions in frame b) illustrate the codomain of the intersection points x_{s0} and x_{s1}, as deduced from the intersection between the parabola and sigmoidal curves for $a = 0$ and $a \to \infty$.

$$\frac{\omega_{(x)}}{\omega_{(x)}^2 + 4x^2} = \frac{4\omega_0}{16\omega_0^2 + 4x^2}$$

or

$$x^2 = \omega_0\,\omega_{(x)} = \frac{2\,\omega_0^2}{1 + \exp(-ax)} = H_{(x)}$$

The solution of the latter transcendent equation is given graphically in Figure 7. From the basic shape of the sigmoidal function and the parabola it is evident that there are two and only two intersection points, x_{s0} and x_{s1}. For all $x < x_{s0}$ and $x > x_{s1}$ the relation $x^2 > 2\omega_0^2/(1+\exp(-ax))$ is true. Thus, $f(x) < G(x)$ is true in the intervals $[-\infty : x_{s0}]$ and $[x_{s1} : \infty]$ and the integral of $f(x)$ is finite there.

Since $f(x)$ has no singularities in the interval $[x_{s0} : x_{s1}]$, the integral of $f(x)$ is finite in the range form $[-\infty : \infty]$.

The latter argument would not hold, if the intersection points x_{s0} and x_{s1} could, for a certain choice of the asymmetry parameter a, diverge to $\pm\infty$. Fortunately, this case can be excluded by the elementary properties of the sigmoidal function and the parabola; the dashed regions in Figure 7 b) illustrate the codomain of x_{s0} and x_{s1} for any choice of a from the interval $[0 : \infty]$. In fact, both intersection points are restricted to finite values.

Gauss We will proceed with the proof of the convergence of the Gaussian part of the asymmetric Pseudo-Voigt in a similar way. Let $f(x)$ be a Gaussian curve, where the asymmetry is specified by the parameters ω_0 and a according to equation (9). The relation of $f(x) \geq 0$ is true for all possible x. Accordingly we choose as majorant a symmetric Gauss curve with the width of $4\,\omega_0$. This configuration is illustrated for $\omega_0 = 1$ in Figure 8 a). As above, we have to work out the intervals where $G(x)$ is larger than $f(x)$. The intersection points of both curves are given by:

$$\frac{1}{\omega_{(x)}}\exp\left(-\frac{x^2}{\omega_{(x)}^2}\right) = \frac{1}{4\,\omega_0}\exp\left(-\frac{x^2}{16\,\omega_0^2}\right)$$

or

$$x^2 = \frac{(2\,\omega_0)^2\,\ln(2+2\exp(-ax))}{3/4+2\exp(-ax)+\exp(-2ax)} = H_{(x)}$$

Since the function $H(x)$ is not as elementary as the corresponding sigmoidal function in the preceding chapter, we will briefly discuss

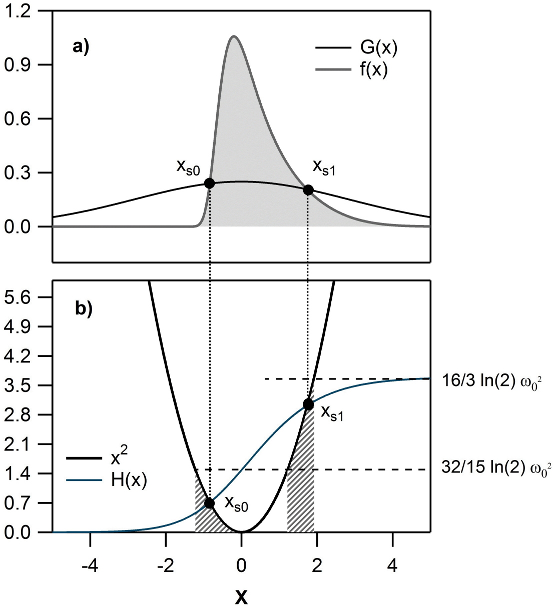

Figure 8. Determination of the intersection points between the asymmetric Gauss profile, $f(x)$ and its majorant curve $G(x)$. The dashed area indicates the codomain of the intersection points as deduced from the intersection of the parabola x^2 with the auxiliary function $H(x)$ for $a = 0$ and $a \rightarrow \infty$.

its properties. Figure 9 illustrates the appearance of $H(x)$ for various asymmetry parameters. It is evident that $H(x)$ closely resembles a sigmoidal function.

The following properties can be derived from the equation:

$$\begin{aligned}
\lim_{x \to -\infty} H_{(x)} &= 0 \\
\lim_{x \to \infty} H_{(x)} &= (16/3)\ \omega_0^2 \ln(2) \\
\lim_{a \to 0} H_{(x)} &= (32/15)\ \omega_0^2 \ln(2) \\
H_{(0)} &= (32/15)\ \omega_0^2 \ln(2)
\end{aligned}$$

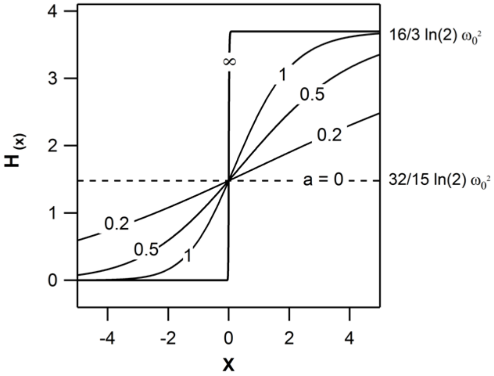

Figure 9. The dependency of $H(x)$ to various asymmetry parameters a. The function can be described as a modified sigmoidal.

After these preparations, we can proceed in discussing the intersection points and the intervals in a similar way as in the latter paragraph. Figure 8 b) illustrates the solution of the transcendental equation. The intersection points between the asymmetric Gauss $f(x)$ and its majorant $G(x)$ can be deduced as the intersection points between the parabola x^2 and $H(x)$. Thus, for the intervals $[-\infty : x_{s0}]$ and $[x_{s1} : \infty]$ the relation $f(x) < G(x)$ is true, and so is $\int f(x)dx < \int G(x)dx$.

Since the integral of $f(x)$ is finite in the interval $[x_{s0} : x_{s1}]$ as well, the integral of $f(x)$ is finite in the range form $[-\infty : \infty]$. As in the preceding chapter, the finiteness of the intersection points ensures a general validity of the given arguments.

Conclusion Since we have shown that the integrals of the Lorentzian as well as Gaussian parts of the asymmetric Pseudo-Voigt function converge, we can conclude that the integral of the Pseudo-Voigt function on the interval $[-\infty : \infty]$ is well defined, just as in the case of symmetric Gaussian and Lorentzian curves. Although its value cannot be given as an analytical function, a numerical integration over a large enough interval will approximate the area from $-\infty$ to ∞ sufficiently.

Application to XPS In the following section, we will see that the reproduction of real asymmetric photoelectron spectra requires that the sigmoidal FWHM function $\omega(x)$ is allowed to shift relatively to the peak position E_0; a further degree of freedom that leads to a further parameter b.

$$\omega_{(x)} = \frac{2\,\omega_0}{1+\exp(-a\,(x-b))} \tag{10}$$

Before proceeding with the applications of Equation (10), we will briefly exemplify the convergence behaviour of the Gaussian part of the resulting Pseudo-Voigt profile. However, we omit a convergence proof of the Lorentzian part since it can be done in an identical way. We will constrain the discussion to values of the asymmetry parameter $a > 0$. In the case of $a = 0$, the shift parameter b has no influence on the curve whatsoever.

As shown in the preceding sections, the intersection points between an asymmetric Gaussian curve and its majorant can be deduced graphically by intersecting the parabola x^2 with an auxiliary function $H(x)$. Applying Equation (10) in the definition of a Gaussian curve, one obtains:

$$\begin{aligned}
\frac{1}{\omega_{(x)}}\exp\left(-\frac{x^2}{\omega_{(x)}^2}\right) &= \frac{1}{4\,\omega_0}\exp\left(-\frac{x^2}{16\,\omega_0^2}\right) \\
\Rightarrow x^2 &= \frac{(2\,\omega_0)^2\,\ln(2+2\exp(-a(x-b)))}{3/4+2\exp(-a(x-b))+\exp(-2a(x-b))}
\end{aligned}$$

The graphical solution for this equation is illustrated in Figure 10 for several choices of b. For decreasing values of b from 0 to $-\infty$, the intersection point x_{s1} approaches its maximum position $x_{s1}^{max} = \sqrt{(16/3)\ln(2)}\ \omega_0$. Similarly, the intersection point x_{s0} approaches its minimum value of $x_{s1}^{min} = -\sqrt{(16/3)\ln(2)}\ \omega_0$. Thus, for all values of $b \in [-\infty : 0]$ the intersection points between the asymmetric Gaussian and its majorant curve are limited to the interval $[-\sqrt{(16/3)\ln(2)}\ \omega_0 : \sqrt{(16/3)\ln(2)}\ \omega_0]$. Outside this interval, the majorant curve is always larger than the asymmetric Gauss curve. This proves that for any choice of $b \in [-\infty : 0]$, the asymmetric Gaussian curve has a finite and unique area.

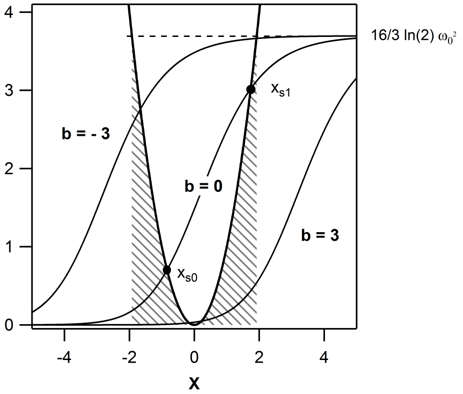

Figure 10. Intersection points of the parabola x^2 and the auxiliary function $H(x)$ – illustrated for various values of b – according to Equation (11). These intersection points are identical to the intersection points between an asymmetric Gauss profile and its majorant curve. The dashed regions mark the codomain of both intersection points x_{s0} and x_{s1}.

We will now consider a choice of b from the interval $[0 : \infty]$ and show the convergence of the area of the asymmetric Gaussian for this case. For a shift of b towards infinity, both intersection points x_{s0} and x_{s1} converge towards $x = 0$.

Thus, for any choice of $b \in [0 : \infty]$, the resulting intersection points will be constrained to the interval $[x_{s0} : x_{s1}]$; outside this interval the majorant is always larger than the asymmetric Gauss curve, irrespective of the choice of b. This proves the convergence of the asymmetric Gaussian curve for all $b \in [0 : \infty]$. Note that for the limit of $b \to \infty$ the asymmetric Gaussian curve approaches the shape of a δ-function.

In summary, we have shown that for any choice of b from $[-\infty : 0]$ and $[0 : \infty]$, and hence for any choice of b from $[-\infty : \infty]$, the profile area remains finite.

Examples In this paragraph we will discuss in particular spectra acquired with synchrotron radiation. Although the present work does not cover synchrotron based measurements, it is important to comment on the general validity of the asymmetric Pseudo-Voigt function, introduced in the latter section. Accordingly, we will use XPS spectra acquired with synchrotron radiation as a benchmark. Prior to peak fitting, a Shirley type background[70] has been subtracted from all spectra presented in this section.

Figure 11 shows a least-squares fit to a spectrum of elemental sulphur on Pd(100), acquired by synchrotron radiation[c]. The fit residual (calculated as difference between the raw data and the fit result) shows in the range of the peak maximum an oscillating behaviour. This numerical phenomenon is characteristic for least-squares fits that use Pseudo-Voigt instead of Voigt curves.[105,106]

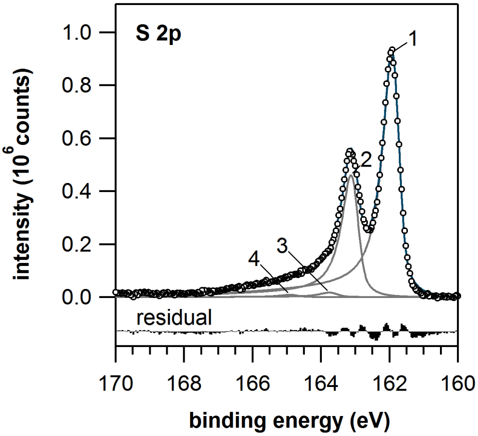

Figure 11. Least-squares fit of the S 2p region of sulphur; the parameters of the peaks 1 - 4 are given in Table 1.

The numerical results of this fit are given in Table 1. The values of the peak area, FWHM, and position exemplify the previous statement that, if asymmetry is present in a photoelectron line, the mere fit co-

---

[c] Courtesy of Dipl.-Phys. Michael Lorenz and M.Sc. Karin Gotterbarm

efficients do not reflect the corresponding physical values any more. However, those values can be extracted numerically from the resulting curves. In Table 1, those quantities are indicated as *measured.*

	Peak			
	1	2	3	4
Area (Parameter)	782300	392300	18640	9504
Area (Measured)	932600	467600	12200	11200
Position (Parameter)	161.97	163.17	163.80	164.95
Position (Measured)	161.93	163.12	163.75	164.90
FWHM (Parameter)	2.51	2.51	2.51	2.51
FWHM (Measured)	0.70	0.70	0.70	0.70
m (Gauss-Lorentz ratio - parameter)	0.68	0.68	0.68	0.68
a (Asymmetry - parameter)	0.92	0.92	0.88	0.88
b (Asymmetry shift - parameter)	2.1	2.1	2.1	2.1
Asymmetry: $1 - \frac{\text{FWHM}_{\text{right}}}{\text{FWHM}_{\text{left}}}$	0.28	0.28	0.28	0.28

Table 1. Numerical parameters of the least-squares fit of the S 2p region of elemental sulphur on Pd(100).

The signals at 161.92 and 163.13 eV (peak 1 and 2), and the peaks at 163.8 and 164.95 eV (peak 3 and 4) comprise each a sulphur 2p doublet. Accordingly, the intensity ratio between peak 1 and peak 2, as well as peak 3 and peak 4, should be 2 : 1, as given by the degeneracies of the $2p_{3/2}$ and $2p_{1/2}$ states. The intensity ratio between peak 1 and 2 is found to be 1.9985 : 1 and the corresponding ratio between peaks 3 and 4 is 1.9887 : 1. The strong deviation of the FWHM coefficient from the actual FWHM of the peaks underlines once more that one should be aware of numerical effects while interpreting the fitting results of XPS data.

As a further example, we will consider a fit to the C 1s spectra of C_2H_2/Pd(100)[d] (Figure 12). This spectrum was chosen, since it comprises a relatively simple sub-structure and shows clearly the characteristic of an isolated peak. In comparison to the example of the last paragraph, the C 1s level appears to be reconstructed in a slightly higher quality than the S 2p spectrum. The oscillation of the fit residuum is significantly smaller than in the previous spectrum. Peaks 2 and 3 presumably represent vibrational excitations of the adsorbed C_2H_2 molecules, while the signal at 286.49 eV possibly originates from traces of carbon monoxide.[109]

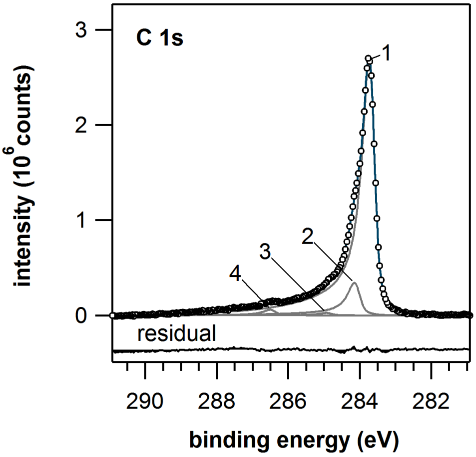

Figure 12. Least-squares fit of the C 1s region of the system C_2H_2/Pd(100) ; the parameters of the peaks 1 - 4 are given in Table 2.

---

[d] Courtesy of M.Sc. Oliver Höfert

	Peak			
	1	2	3	4
Area (Parameter)	1847000	234400	17580	40590
Area (Measured)	2145000	272200	20420	47130
Position (Parameter)	283.78	284.19	284.97	286.55
Position (Measured)	283.75	284.15	284.93	286.49
FWHM (Parameter)	1.52	1.52	1.52	1.52
FWHM (Measured)	0.54	0.54	0.54	0.54
m (Gauss-Lorentz ratio - parameter)	0.76	0.76	0.76	0.76
a (Asymmetry - parameter)	1.79	1.79	1.79	1.79
b (Asymmetry shift - parameter)	0.9	0.9	0.9	0.9
Asymmetry: $\mathbf{1-\frac{FWHM_{right}}{FWHM_{left}}}$	0.33	0.33	0.33	0.33

Table 2. Numerical parameters of the least-squares fit of the C 1s region of the C_2H_2/Pd(100) system.

As a final example, we will demonstrate a least-squares fit to the Pd 3d region, acquired from a sample covered with Pd nanoparticles [P7]. In contrast to the latter examples, this spectrum was recorded with a regular, monochromatized Al Kα X-ray source. The raw data (Figure 13) were modeled with three peaks; two representing the $3d_{5/2}-3d_{3/2}$ doublet, while the third can be attributed to plasmon excitations.[111] As above, we can use the reproduction of the nominal intensity ratio of the doublet as a benchmark for the quality of the fit. The procedure resulted in an intensity ratio between the $3d_{5/2}$ and $3d_{3/2}$ components of $1.504:1$, in close agreement to the nominal ratio of $1.5:1$. The fit results, listed in Table 3, underline again that if asymmetry is applied in a fitting procedure, the fit coefficients do not represent the corresponding physical quantities any more, but merely describe the shape of the curve. The oscillating behaviour of the fit-residual is comparable to the S 2p fit above. The relatively high value of the parameter b, representing a strong shift of the corresponding sigmoidal function, exemplifies the necessity of this degree of freedom for a satisfying fit result.

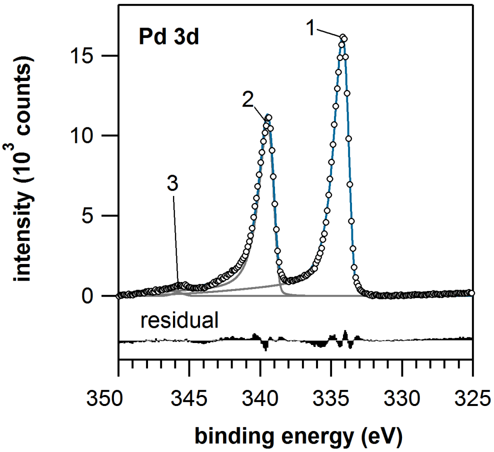

Figure 13. Pd 3d signal, recorded with a standard lab source; the numerical results are given in Table 3.

	Peak		
	1	2	3
Area (Parameter)	23680	15740	229
Area (Measured)	29480	19600	229
Position (Parameter)	334.31	339.60	345.79
Position (Measured)	334.20	339.49	345.80
FWHM (Parameter)	5.88	5.88	1.02
FWHM (Measured)	1.54	1.54	1.04
m (Gauss-Lorentz ratio - parameter)	0.15	0.15	0.15
a (Asymmetry - parameter)	0.44	0.44	0.1
b (Asymmetry shift - parameter)	4.7	4.7	0
Asymmetry: $1 - \frac{\mathrm{FWHM_{right}}}{\mathrm{FWHM_{left}}}$	0.35	0.35	0.35

Table 3. Fit results of a Pd 3d spectrum fitted with the novel fit function.

Summary In this section, we have shown that the introduction of a sigmoidal FWHM function into a regular Pseudo-Voigt function has various advantages. The application of the function

$$\begin{aligned}\text{Pseudo-Voigt} &= (1-m)\sqrt{\frac{4\ln 2}{\pi}}\,\frac{A_g}{\omega_{(x)}}\,e^{-4\ln 2\left(\frac{x}{\omega_{(x)}}\right)^2}\\ &\quad +m\,\frac{A_l}{2\pi}\,\frac{\omega_{(x)}}{(\omega_{(x)}/2)^2+x^2}\end{aligned}$$

with

$$\omega_{(x)} = \frac{2\,\omega_0}{1+\exp(-a\,(x-b))}$$

in least-squares fits of asymmetric spectra results in a good reproduction of the experimental curves and stoichiometric relations. But, more importantly, the numerical properties of this approach guarantee a finite and well defined area of the fit curves, thus no arbitrary integration cutoff criteria have to be applied. This property makes it feasible to compare curves with different asymmetry and a different FWHM in an unambiguous way.

2.1.6 Investigating valence levels with UPS

After the discussion of the most relevant aspects of XPS, we will now continue elucidating some relevant facts concerning UV photoelectron spectroscopy. In contrast to XPS, UV photoelectron spectroscopy is not suitable to acquire quantitative information on the chemical composition of a sample. This is mainly due to a substantial variation of photoionization cross sections of different energy levels. Furthermore, diffraction effects of photoelectrons at very low kinetic energies can not be excluded. In the context of the present work, however, UPS was used for the following applications:

(i) Show the presence of adsorbate-substrate valence states.

(ii) Measure work-function changes $\Delta\phi$ of the sample upon deposition of adsorbates.

(iii) Follow adsorbate-induced modifications of substrate surface states.

(iv) Monitor the modification/creation of valence states by interfacial chemical reactions.

While most of those aspects follow directly from features in the observed spectra, the modus operandi for the determination of the work function ϕ, and its changes, possibly needs a brief explanation. Figure 5 a) shows an UPS survey spectrum of a clean Au(111) surface, acquired with HeI radiation (21.2 eV). It is apparent that the spectral cut-off, which represents electrons with the highest sampled binding energy, is well below 21.2 eV, the value which could be expected at a first sight. The reason for this finding is that even electrons with a binding energy of 0 eV, i.e., those directly at the Fermi edge, require a certain amount of energy to be released from the solid. This energy is commonly referred to as *work function* ϕ. Thus, the energy required to excite a photoelectron is actually the sum of the binding energy (measured relative to the Fermi edge) and the work function of the sample. Therefore, the energy provided by a 21.2 eV photon can only excite electrons with a binding energy up to $E_{bind}^{max} = 21.2\ \text{eV} - \phi$. Accordingly, by measuring the maximum binding energy position as the distance from the spectral cut-off to the Fermi edge (Figure 5 a), one can directly calculate the work function ϕ. Adsorbate-induced work function changes that result in a shift of the spectral cut-off, can thus be quantified accordingly[e]. Typical values for work functions are in the range of several electron volts, for a gold(111) sample ϕ equals ca. 5.4 eV.

2.1.7 Further reading

Since a comprehensive discussion of all aspects of photoelectron spectroscopy would be far beyond the scope of the present work, it appears necessary to refer the interested reader to further literature. A thorough discussion of photoelectron spectroscopies, with a modern focus on theoretical aspects is to be found in the textbooks of Hüfner[72] and Briggs and Seah.[112] A more experimental approach can be found in

---

[e] The photoelectrons at the spectral cut-off have a very low kinetic energy; to avoid scattering effects or artefacts due to the spectrometer, those electrons have to be accelerated towards the spectrometer. Commonly, applying a bias of -5 V to the sample is sufficient for this purpose.

the textbook of Grasserbauer[98] together with a short introduction to electron spectrometers. The electron spectrometer used in this work is described in the paper of Gelius et al.,[113] while the basic design of electron spectrometers is described in an article of Roy[114]. Since an electron spectrometer is principally based on an array of electrical lenses, it appears necessary to mention the textbook of Grosser[115] on this topic.

2.2 Low-Energy Electron Diffraction – LEED

Since Low-Energy Electron Diffraction (LEED) was utilized to control the long-range order of the Au(111) and Ag(111) single-crystal surfaces, and, on some occasions, the long-range order of tetrapyrrole monolayers, we will briefly review this method. We will develop a principal understanding of this experimental tool based on the mathematics of the Fourier transformation. LEED is performed by irradiating sample surfaces with low energetic electrons with a kinetic energy in the range between tens and several hundreds of electronvolts. According to fundamental quantum mechanical principles, we can interpret the ensemble of impinging electrons as a plain wave. This wave is scattered and reflected as it hits a sample surface,[f] placed perpendicular to its initial direction of propagation. Following the principle of Huygens, each atom or molecule on the surface acts then as a point source for a scattered wave. The sum over all point sources results in an interference pattern that can be observed experimentally by installing a luminescent screen in front of the sample. This diffraction pattern has in fact a close connection to the spatial distribution of the scattering objects on the sample. Under the approximation of Fraunhofer diffraction[116], it represents the Fourier transformed of the scattering surface structure.[1,116,117] If this surface structure has a periodicity, i.e., if the scattering occurs on a two-dimensional lattice, its Fourier transformed will show a corresponding characteristic structure. The interpretation of the structures in the Fourier transformed is possible in a straight-forward way, since it can be shown that the

---

[f] In a first-order approximation it is justified to neglect the scattering on bulk atoms due to the low mean free path of electrons in solids. Thus the scattering only occurs at the very first atomic layer.

Fourier transformed of a lattice is identical to its *reciprocal lattice.*[118] Hence, LEED experiments allow to directly image the reciprocal lattice of a sample surface, and thus to draw conclusions on the surface lattice itself.

In the following section, we will briefly discuss the key result that the Fourier transformed (and hence the Fraunhofer diffraction pattern) of a lattice is identical to its reciprocal lattice. The proof will be given for the more general case of a three-dimensional lattice, including the scattering on a two-dimensional surface net, as it is observed in LEED measurements. We will take for granted that the diffraction pattern is identical to the Fourier transformed and show that the Fourier transformed is identical to the reciprocal lattice.

We will start our discussion with the case of an one-dimensional lattice, i.e., a regular, infinite chain of atoms. Mathematically, this chain of atoms (mutual distance a) can be expressed as a series of δ-functions.

$$\sum_{n=-\infty}^{\infty} \delta(x-na)$$

Such a function is often referred to as *comb(x).*[116] The Fourier transformed of this equation is by itself a series of δ-functions, however, in k-space and with an inverted periodicity.[116,118]

$$\int \left(\sum_{n=-\infty}^{\infty} \delta(x-na) \right) \exp(ikx)\, dx \;=\; \sum_{n=-\infty}^{\infty} \delta(k-2\pi n/a) \qquad (11)$$

Extending our considerations to a three-dimensional lattice, we may use the lattice vectors $\vec{a}$, $\vec{b}$, and $\vec{c}$ as a basis.

$$\vec{r} = r_a\vec{a} + r_b\vec{b} + r_c\vec{c}$$

Accordingly, we can describe the lattice by an array of δ-functions in the following way:

$$\sum \delta(r_a - n_a a) \sum \delta(r_b - n_b b) \sum \delta(r_c - n_c c) \qquad (12)$$

Similarly, the $\vec{k}$-vector required for the Fourier transformed can be written as

$$\vec{k} = k_A\vec{A} + k_B\vec{B} + k_C\vec{C}$$

where the length and orientation of the three basis vectors in not specified yet. We will show now that the three-dimensional Fourier transformed of Equation (12) can be calculated in a straight-forward manner, if the basis vectors $\vec{A}$, $\vec{B}$, and $\vec{C}$ are chosen in an advantageous way.

$$\int_c \int_b \int_a \left(\sum \delta(r_a - n_a a) \sum \delta(r_b - n_b b) \sum \delta(r_c - n_c c) \right) \dots \qquad (13)$$

$$\dots \times \exp(i\vec{k}\vec{r})\; dr_a\; dr_b\; dr_c$$

For any other choice, the resulting Fourier transformed will have the same appearance, but the computation process and the resulting equations appear more difficult.

The exponential term in Equation (13), in particular the product $\vec{k}\vec{r}$, has generally the effect that one cannot rewrite the threefold integral (13) as a product of three one-dimensional integrals, which would be favourable for the analytical solution. However, it is possible to find a certain set of basis vectors of k-space $\vec{A}$, $\vec{B}$, and $\vec{C}$ that allows to perform this operation, and thus obtain the solution of the threefold integral. The product $\vec{k}\vec{r}$ writes as

$$\begin{aligned}
\vec{k}\vec{r} \quad = \quad & \vec{A}\vec{a}k_A r_a + k_A\vec{A}\,(\vec{b}r_b + \vec{c}r_c) + \\
& \vec{B}\vec{b}k_B r_b + k_B\vec{B}\,(\vec{c}r_c + \vec{a}r_a) + \\
& \vec{C}\vec{c}k_C r_c + k_C\vec{C}\,(\vec{a}r_a + \vec{b}r_b)
\end{aligned}$$

At this point, vector $\vec{A}$ is chosen to be perpendicular to the lattice vectors $\vec{b}$ and $\vec{c}$; in other words, $\vec{A}$ is chosen parallel to $\vec{b} \times \vec{c}$. This results in $\vec{A}\vec{b} = \vec{A}\vec{c} = 0$. Proceeding in a similar way and choosing $\vec{B}$ perpendicular to $\vec{a}$ and $\vec{c}$, and $\vec{C}$ perpendicular to $\vec{a}$ and $\vec{b}$, we obtain:

$$\vec{k}\vec{r} = \vec{A}\vec{a}k_A r_a + \vec{B}\vec{b}k_B r_b + \vec{C}\vec{c}k_C r_c$$

Introducing this in the exponential function of the Fourier transformation leads to

$$\exp(i\,\vec{k}\vec{r}) = \exp(i\,\vec{A}\vec{a}k_A r_a)\,\exp(i\,\vec{B}\vec{b}k_B r_b)\,\exp(i\,\vec{C}\vec{c}k_C r_c)$$

It is possible to achieve a further simplification by restricting the lengths of the vectors $\vec{A}$, $\vec{B}$, and $\vec{C}$ such that $\vec{A}\,\vec{a} = \vec{B}\,\vec{b} = \vec{C}\,\vec{c} = 1$. Then, the Fourier integral (13) can be factorised into three one-dimensional integrals, each of the form of Equation (11).

$$\left(\int_a \sum \delta(r_a - n_a a) \exp(i\, k_A r_a)\, dr_a\right) \left(\int_b \sum \delta(r_b - n_b b) \exp(i\, k_B r_b)\, dr_b\right) \ldots$$
$$\ldots \times \left(\int_c \ldots\, dr_c\right)$$

Hence, the result can be written in the form

$$\sum_{n=-\infty}^{\infty} \delta(k_A - 2\pi n/a) \sum_{n=-\infty}^{\infty} \delta(k_B - 2\pi n/b) \sum_{n=-\infty}^{\infty} \delta(k_C - 2\pi n/c) \quad (14)$$

where the first factor is a sequence of δ-functions along the direction of $\vec{A}$, the second along $\vec{B}$, and the third along $\vec{C}$. The mutual distance of the δ-functions is $2\pi/a$, $2\pi/b$, and $2\pi/c$ respectively. The two constraints $\vec{A} \mid\mid (\vec{b} \times \vec{c})$ and $\vec{A}\,\vec{a} = 1$ can be expressed simultaneously with the equation

$$\vec{A} = \frac{\vec{b} \times \vec{c}}{\vec{a}\ (\vec{b} \times \vec{c})} \quad (15)$$

This relation is precisely the definition of a reciprocal lattice vector.[g] Thus, Equations (14) and (15) reflect the point-distance and orientation within the reciprocal lattice. Similar conclusions can be drawn for $\vec{B}$ and $\vec{C}$. Thus, we have shown that the Fourier transformed of a lattice is identical to its reciprocal lattice.

A further discussion of LEED, from a more experimental point of view, can be found in the textbooks of Zangwill[117], or Henzler and Göpel[1].

2.3 Low-Energy Ion Scattering Spectroscopy – LEIS

In contrast to photoelectron spectroscopy, Ion Scattering Spectroscopy (ISS or LEIS) is only sensitive to the atomic composition of the topmost atomic layer and no information concerning the chemical state

---

[g] This definition matches the definition which is commonly used in crystallography; however, in solid state physics it is more common to define the reciprocal lattice based on $\vec{A}\vec{a} = \vec{B}\vec{b} = \vec{C}\vec{c} = 2\pi$. Thus, the definitions differ by a factor of 2π, resulting in $\vec{A}_{solidState} = 2\pi \times \vec{A}_{cryst.}$.[119]

of the atoms can be derived. In an ISS measurement, an ion-beam is scattered on surface atoms. Considering an elastic collision between the ions and the surface atoms, one can derive the residual energy of the ions after the collision. Its value is a function of (i) the initial energy of the ions, (ii) the mass of the ions and the surface atoms, and (iii) the scattering angle, according to the following equation:

$$E_f = E_i \frac{\left(\cos\Theta + \sqrt{(m_{atom}/m_{ion})^2 - \sin^2\Theta}\right)^2}{(1 + m_{atom}/m_{ion})^2}$$

The backscattered ions posses, due to energy and momentum conservation, a well defined residual energy, which is given by their initial kinetic energy, their mass, the mass of the scattering partner, and the scattering angle. Their kinetic energy distribution shows a sharp peak.

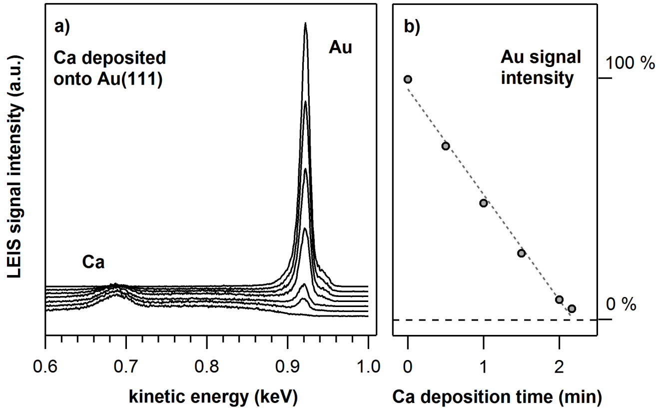

Figure 14. 1 keV He LEIS spectra of a deposition series of Ca onto Au(111); the peak at a kinetic energy of 920 eV originates from elastic collisions with Au atoms, the peak at 690 eV from collisions with Ca atoms.

Applying the latter equation, it is possible to calculate from the position of this peak the atomic mass of the scattering partners on the surface, and thus identify their atomic species. In the present work, ISS was mainly used as a deposition monitor. This is possible due to the fact that effectively only the topmost atomic layer contributes to the ISS signal. If, in a deposition series, the substrate intensity dropped by 50%, one can directly conclude that only 50% of the substrate surface remain uncovered by the adsorbate. For illustration, Figure 14 shows LEIS spectra, acquired during the deposition of Ca onto a Au(111) surface. Due to the fact that only the upmost atomic layer contributes to LEIS signals, it follows that a closed layer of an adsorbate shows the same intensity as a bi- or multilayer. Thus, LEIS experiments are less suitable for multilayer deposition experiments. For further reading please be referred to the works of Niehus[120,121] or the textbook of Henzler and Göpel[1].

3 Results

The results presented in this chapter were acquired with photoelectron and ion spectroscopies. It should be noted, however, that the corresponding publications were partly done in cooperation with other groups and thus contain additional information acquired by different experimental methods. The following section gives a brief survey of the most essential results from the publications [P1] - [P7].

3.1 Coordination chemistry of metallotetrapyrroles on Ag(111) and Au(111) surfaces

3.1.1 Cobalt(II) phthalocyanine adsorbed on Ag(111) [P1]

The adsorption of cobalt(II) phthalocyanine (CoPc) on Ag(111) was examined with XPS and UPS. From previous investigations, a substantial modification of the electronic states of the central cobalt atom was to be expected;[33] thus, the aim of the article [P1] was to further elucidate details of this coupling. In particular, the modification of the Co 2p core levels contains much more information than one would expect at the first glance. The cobalt 2+ ion in CoPc possesses an unpaired electron in its 3*d* sub-shell, corresponding to a molecular spin of S=1/2. Since cobalt 2+ ions also occur with a net-spin of S = 3/2, CoPc is referred to as Co(II) low-spin complex. Due to this open shell-character, multiplet effects can be observed in the cobalt core levels. Briefly, such multiplet effects arise if the unpaired spin of the core-hole after photoionization couples to the spin of the unpaired electrons in outer shells. Hence, one can find for instance multiple lines in an *s* core-state, but also in all other core level signals. It was shown for cobalt that each spin configuration has an individual spectral fingerprint in the 2p region.[15,90,92] The multilayer spectrum in Figure 15 exhibits a typical Co(II) S = 1/2 pattern. The apparent spin-orbit splitting is with 15.7 eV significantly larger than in metallic cobalt and the shape of the peaks suggests the presence of an unresolved sub-structure; nevertheless, the intense satellite structures of Co(II) high-spin complexes are absent. A least-squares fit of the Co 2p region of the CoPc multilayer is shown in Figure 16. The relative

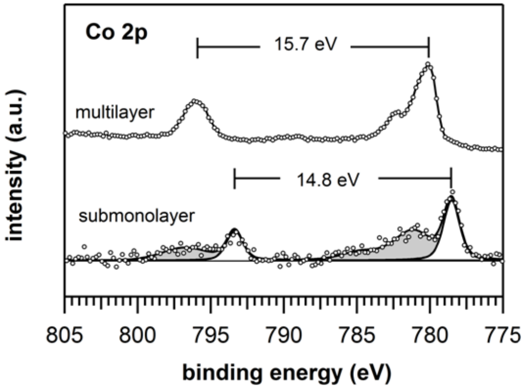

Figure 15. Co $2p_{3/2}$ spectra of a CoPc multilayer and submonolayer on Ag(111). The background subtraction of the submonolayer spectrum was performed in a way that the ratio between the total $2p_{3/2}$ and $2p_{1/2}$ intensities, i.e. including the gray-shaded satellite features, matches the nominal value of 2 : 1. Reprint from [P1].

intensities of the individual peaks have been constrained to the nominal values given by the degeneracy of corresponding J states, in line with the interpretation of Frost[15,90] and Briggs[92]. Interpreting the feature at 782.5 eV as a satellite, due to a spin-dependent process, its relative intensity is in accordance with theory.[16] One has to note that the latter mechanism results possibly in different satellite structures for the $2p_{3/2}$ and $2p_{1/2}$ levels. However, alternatively the feature at 782.5 eV was associated with further multiplet peaks.[92]

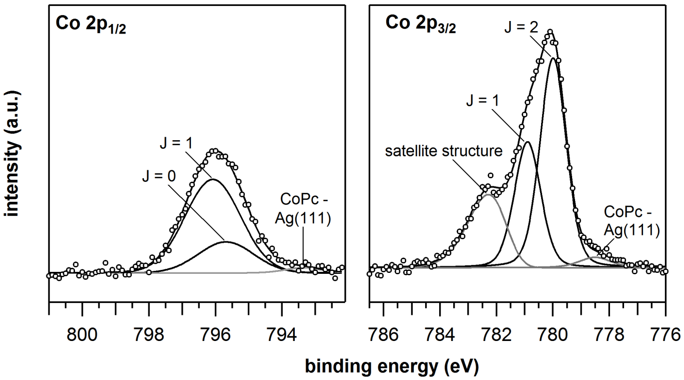

Figure 16. Least-squares deconvolution of the Co 2p region, recorded from a cobalt(II) phthalocyanine multilayer. The relative intensities of the photoelectron lines were constrained to the values given by the degeneracy of the corresponding J states. The existence of those states results from a coupling of the spin-orbit j = 3/2 and j = 1/2 states with the S = 1/2 state of the d-electrons. The angular momentum of the d electrons was assumed to be quenched by the ligand field of the phthalocyanine macrocycle. The relative intensity of the satellite in the $2p_{3/2}$ spectrum matches the value given by Borod'ko.[16] See text and [P1] for details.

A more detailed analysis of the shape of 2p core levels of CoPc (sub-)monolayers and comparison to the well known 2p line patterns of different cobalt spin states reveals that the molecules in direct contact to the Ag(111) substrate are in a diamagnetic state. The spin-orbit separation is identical to the value obtained for diamagnetic Co(0), or Co(III) compounds. The absolute binding energy positions are close to Co(0) values. Those findings confirm previous DFT calculations that predict a charge transfer from the substrate to the cobalt ions, associated with a quenching of the molecular spin.[122] The complete removal of any multiplet effects from the CoPc monolayer spectrum is further corroborated by the fact that the ratio between the FWHM of the Co $2p_{3/2}$ and $2p_{1/2}$ components, as determined by the additional broadening of the $2p_{1/2}$ level due to the Coster-Kronig process, is in agreement with literature values.[77,78] UPS measurements of the valence levels of CoPc monolayers resulted in the observation of a doublet-like peak structure close to the Fermi energy, as previously anticipated with DFT.[122] The latter results further confirm the current theoretical understanding of the interaction between Co-tetrapyrroles and the Ag(111) surface.

3.1.2 Co(II) and Fe(II) tetrapyrroles on Au(111) [P2, P3]

In the previous chapter, it was shown that the interaction between cobalt tetrapyrroles and an Ag(111) surface can be understood in terms of a charge transfer from the substrate to the central metal ion of a porphyrin or phthalocyanine. In the following, we will discuss the corresponding situation on an Au(111) interface. One of the most significant differences between the Ag(111) and Au(111) surfaces, apart from chemical aspects, is their fundamentally different surface morphology due to the reconstruction of the Au(111) surface. The upmost atomic layer of gold atoms suffers an uniaxial compression along a $[1\bar{1}0]$ direction; as a consequence, 23 surface atoms occupy 22 bulk sites, leading to a geometrical mismatch between the surface lattice and the bulk structure below. Thus, a periodical alternation of fcc and hcp sites is generated on the surface. The pattern is further complicated since, on a larger length scale, a periodic change of the direction of compression by $\pm$ 120°can be observed. This leads to the herringbone appearance of the reconstructed Au(111) interface, a morphological feature which is still present after the adsorption of tetrapyrrole monolayers.[123,124] Figure 17 a) shows the LEED pattern of a clean Au(111) surface. The hexagonal fine-structure around each spot directly reflects the herringbone reconstruction (6 fold symmetry due to the 120° herringbone variation).

The rich LEED pattern of a Fe(II) phthalocyanine (FePc) monolayer on Au(111) is displayed in Figure 17 b). Such structures are typical for ordered organic adsorbates on Au(111) or Ag(111) substrates.[125] The presence of the pronounced fine-structure indicates a long range order of the film, since short distances in the reciprocal lattice, as imaged by LEED, correspond to long-range periodicities in the real-space lattice of the surface.[125] FePc forms a commensurate adsorbate structure on Au(111) without lifting the herringbone reconstruction of the surface, as previously shown with STM.[123] The LEED pattern observed in our experiments confirms this picture. While the morphology of the FePc films bears no further difficulties, the electronic structure appears more complicated. In comparison to FePc films on Ag(111), where, analogous to CoPc, the adsorbate/substrate interaction led to a shifted and more narrow $2p_{3/2}$

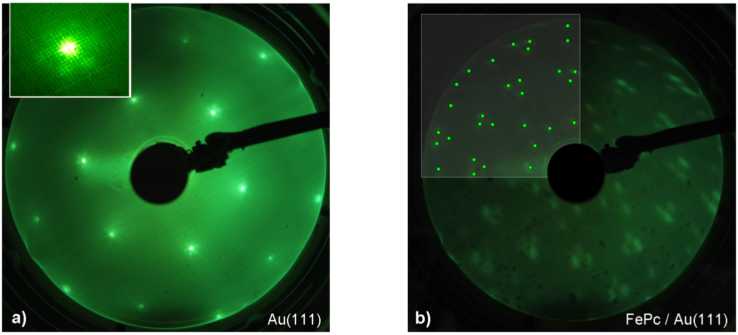

Figure 17. LEED images of a) clean Au(111) after the standard cleaning process and b) a FePc monolayer prepared by multilayer desorption. The inset in a) shows a magnified Au(111) LEED spot; the six fold symmetry reflects the rotational domains (120 °) of the herringbone reconstruction. The complex spot pattern in b) is typical for long-range ordered adsorbate structures. For clarity, the inset in b) shows a schematic drawing of the acquired spot pattern.

signal pattern, the Fe 2p core levels acquired from monolayers on Au(111) show an even higher degree of complexity than observed in the corresponding multilayer spectra. [P2] While the major part of the Fe $2p_{3/2}$ signal from the monolayer is virtually identical to the multilayer spectrum, a minor signal contribution ($\approx 20\ \%$) appears at a lower binding energy, close to a Fe(0) position. This additional component was previously observed with synchrotron radiation.[126,127] In order to deduce whether this line pattern occurs exclusively in Fe(II) phthalocyanine monolayer spectra, or represents a more general phenomenon, comparative measurements have been performed on in-situ prepared Fe(II) tetraphenylporphyrin (FeTPP) and Fe(II) octaethylporphyrin (FeOEP) monolayers. Since the Fe $2p_{3/2}$ spectra of all three compounds exhibit the shoulder at low binding energies, as illustrated in Figure 18, the morphology of the tetrapyrrole ligand seems to have only a minor influence to the observed effect. A close investigation of the valence levels of the tetrapyrrole films revealed the presence of further valence states due to the presence of the iron

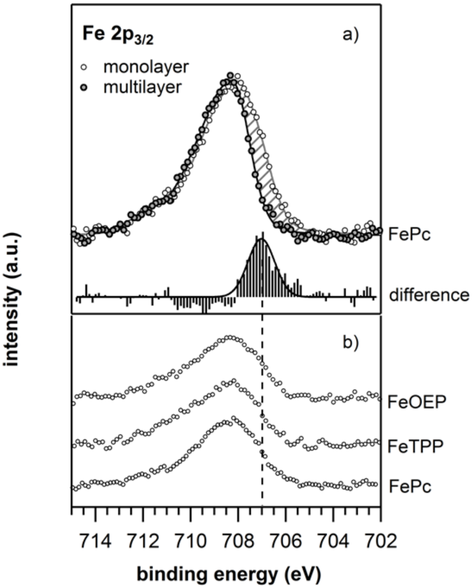

Figure 18. Fe $2p_{3/2}$ spectra of FePc, FeTPP, and FeOEP films on Au(111). Reprint from [P2].

metal center and a complete depopulation of the Au(111) Shockley-type surface state.

Similar experiments with Co(II) tetraphenylporphyrin (CoTPP) and Co(II) octaethylporphyrin (CoOEP) [P3] led to results that follow the same trend as in the case of the Fe compounds. The Co $2p_{3/2}$ shows a minor signal contribution ($\approx 20\%$) at a typical Co(0) position. Again, the morphology of the tetrapyrrole ligand seems to have no significant impact.

This finding, in combination with the close similarity between the results acquired from cobalt and iron tetrapyrrole films, suggests that the reason for the observed complex Fe and Co peak patterns is to be found in the properties of the Au(111) substrate. The most obvious difference between the Ag(111) and Au(111) surface is the more complex surface structure of Au(111), resulting in a variety of different adsorption sites. It appears reasonable that some of those adsorption sites favor a strong interaction between adsorbate and substrate, responsible for the minor peak contribution at the Fe(0) and Co(0) positions, while others only allow a weak coupling, associated with the multilayer-like appearance of the major part of the signal. Such adsorption site effects are well known in the literature on metallotetrapyrroles on Ag(111) or Au(111).[128,129] A detailed discussion can be found in [P2] and [P3].

3.2 Chemical reactions at the organic/metal interface

3.2.1 Covalently linked adsorbate structures on Ag(111) [P4, P5]

Terephthaloyl chloride (TPC)
Ia

p-Phenylene dicarbonyl (pPDC)
Ib

Figure 19. Terephthaloylchloride and its decomposition fragment *p*-phenylene dicarbonyl, (pPDC). Reprint from [P4].

The results presented in this paragraph have been acquired in close cooperation with Dr. Christoph Schmitz (University of Bonn), who provided all STM data in the corresponding articles. The publications [P4] and [P5] were aimed to clarify: (i) the adsorption behavior of terephthaloylchloride on Ag(111) and (ii) the reaction mechanism in the interfacial formation of poly(*p*-phenylene-terephthalamide), PPTA, by the co-adsorption of *p*-phenylenediamine, PPD. Halogen substitued organic compounds have been used as molecular building blocks in the synthesis of surface confined, two-dimensional covalently interlinked adsorbate structures.[38–41] While a heating step is required on Au(111) substrates to cleave the corresponding C – halogen bond, in order to initialize the polymerization reaction,[38] a different situation is to be expected on Ag(111) substrates. There, in particular C – I bonds are reported to dissociate even at relatively low temperatures, resulting in the formation of metastable radical fragments. Upon further heating, those fragments sometimes desorb associatively, i.e., after forming volatile molecules.[44,45] In our study ([P4]), a thin multilayer of terephthaloylchloride was vapor deposited onto an Ag(111) surface at 110 K. During stepwise heating of the sample surface, substantial modifications of the adsorbate became evident. Starting at a temperature of 120 K, shortly before the onset of multilayer desorption, a strongly shifted Cl species arose in the XPS Cl 2p spectra. Its binding energy matches the value reported for chemisorbed Cl on silver surfaces. Additionally, C – halide bonds of molecules adsorbed on Ag samples are typically cleaved in this temperature range.[44,45] Thus, the new, strongly shifted component in the Cl 2p spectra was assigned to isolated chlorine atoms on the Ag(111) substrate. Upon further heating (up to 400 K), a desorption of the TPC multilayer and a complete conversion of the Cl 2p spectrum into the strongly shifted component was observed. Since the photoelectron spectra of the other atomic species, i.e., carbon and oxygen, were subject only to minor modifications, it can be concluded that the remaining molecular fragments do not suffer further decomposition. It was shown by DFT calculations that the resulting pPDC radicals (Figure 19) can adopt several stable adsorption geometries on the Ag(111) substrate, each associated with the formation of covalent bonds between the fragment and the Ag(111) interface; those findings explain the residence of the molecular fragments even at elevated temperatures up to 400 K. On the basis of our data, it cannot be excluded that adjacent pPDC units undergo polymerization reactions at elevated temperatures.

The co-adsorption of TPC with *p*-phenylenediamine was reported to result in the formation of covalently interlinked chains of poly(*p*-phenylene-terephthalamide).[42] In solution, this reaction is known to proceed via a nucleophilic attack, involving the TPC carbonyl and PPD amine groups and resulting in a release of HCl.[43] The results in the previous paragraph suggest a different mechanism on the Ag(111) substrate. At room temperature, the polymerization reaction is initiated by a C-Cl bond cleavage in adsorbed TPC molecules, followed by a reaction of the pPDC radical with the amine groups of co-adsorbed PPD. It should be noted that XPS spectra acquired during the co-deposition of TPC and PPD clearly show the formation of an amide group, corroborating the formation of poly(*p*-phenylene-terephthalamide).[P5] The hydrogen atoms released during the formation of the amide groups may reside on the substrate or desorb associatively as H_2, however, further studies are necessary to address this question.

3.2.2 The interface calcium/rr-poly(3-hexylthiophene) [P6]

The technologically relevant metal/semiconductor interface formed by Ca and regioregular poly(3-hexylthiophene), rr-P3HT, was investigated with XPS and LEIS. The aim of the respective publication [P6] is to demonstrate an experimental route towards better defined, i.e., sharper, interfaces between Ca and rr-P3HT, where subsurface diffusion of Ca should be quenched as far as possible. The fruitful cooperation with Dr. Fabian Bebensee, currently at the University of Aarhus (Denmark) is gratefully acknowledged.

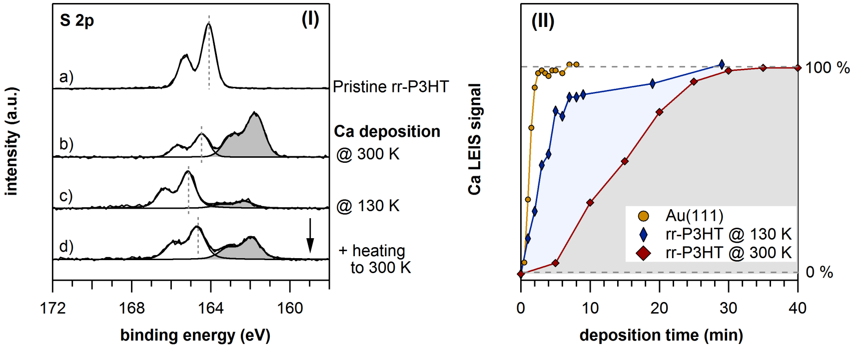

Figure 20. Reaction between P3HT and adsorbed Ca, monitored with XPS and LEIS. Frame (I) illustrates the S 2p region in pristine and Ca-covered rr-P3HT samples. The gray shaded contribution represents a reacted sulphur species; its amount depends on the sample temperature during deposition. The binding energy shifts indicated by the dashed lines are due to band-bending effects, see text for details. All XP spectra have been acquired under an angle of 70 °, in order to achieve a high surface sensitivity. Frame (II) illustrates the Ca deposition time required for a closed saturated layer on Au(111), and rr-P3HT at 130 K and 300 K.

The sample preparation is described in detail in [P6], and in the articles by Zhu[51] and Bebensee[130]. Briefly, approximately 100 nm thick films of rr-P3HT were spin coated on an Al foil, subsequently Ca has been vapor-deposited under UHV conditions from a Knudsen cell. Figure 20 (I) illustrates the sulphur 2p region acquired from: pristine rr-P3HT (curve a), samples with Ca deposited at 300 K onto the rr-P3HT surface (curve b), Ca deposited at 130 K (curve c), and Ca deposited at 130 K followed by subsequent heating to 300 K (curve d).

While the pristine rr-P3HT sample shows only a single S 2p doublet at 164.1 eV ($2p_{3/2}$ signal), the Ca covered samples exhibit a further sulphur 2p doublet, located $\approx$ 2.7 eV below the pristine $2p_{3/2}$ signal. This contribution has been associated with a formation of CaS upon the diffusion of Ca atoms into the P3HT bulk.[51,130] After deposition of Ca at 300 K, the major sulphur 2p signal originates from this chemical species. The corresponding Ca 2p spectrum is depicted in Figure 21, upper curve. The diffusion length up to which CaS is formed was estimated to approximately 3 nm.[51,130] The shift of the S 2p doublet corresponding to pristine thiophene units in curves b) to d) (Figure 20) can be interpreted as a direct evidence for band-bending effects.[117,131]

Lowering the sample temperature during deposition to 130 K resulted in two effects: first, a substantial reduction of the amount of reacted sulphur, and second, a stronger shift of both S 2p doublets to higher binding energies. Figure 21 illustrates the corresponding Ca 2p spectrum; at 130 K the deposited Ca has a strong metallic character, as evident from the pronounced asymmetry and the binding energy of the Ca $2p_{3/2}$ and $2p_{1/2}$ states. The lower mobility of Ca atoms at 130 K suppressed the formation of CaS and thus resulted in the formation of a metallic Ca phase.

The LEIS data displayed in Figure 20(II) confirm this interpretation. Compared to the deposition onto the rr-P3HT sample at 300 K, a substantially smaller amount of Ca was necessary to reach a LEIS signal saturation at a sample temperature of 130 K. This corroborates the interpretation that at 130 K the Ca atoms diffuse to a smaller extent into the bulk polymer; instead they form clusters and eventually a closed layer of Ca on the sample surface. One should note that the suppressed subsurface diffusion is associated with the highest degree of metallic character of the Ca layer and the most pronounced band-bending effects, observed in this study. One could speculate on a direct relation between the sharpness of the interface and the metallic character of Ca layer to the strength of band-bending effects.[117,131]

After heating the sample from 130 K to 300 K, a partial diffusion of Ca atoms into the rr-P3HT matrix sets in, albeit to a significantly smaller amount compared to the Ca deposition at 300 K, as evident from the corresponding S 2p spectrum (curve d in Figure 20). The lower contribution of reacted sulphur and the more pronounced band bending effects (compared to curve b) point towards a sharper defined interface between Ca metal and rr-P3HT, even after allowing the sample to reach room temperature. A control experiment after 12 h at 300 K showed identical results.

Since the least-squares fit to the Ca 2p region, as displayed in Figure 21, is not included in the publication [P6], it will be discussed in more detail at this point.

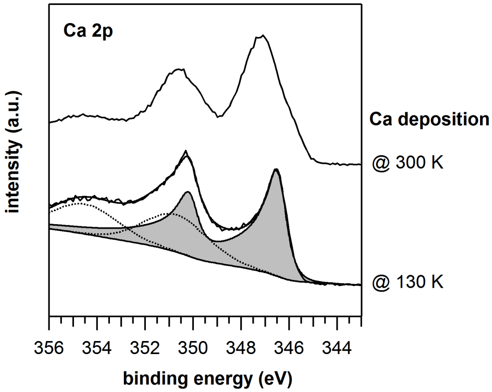

Figure 21. Ca deposited at different temperatures onto the polymer rr-P3HT; the numerical deconvolution of the low-temperature spectrum is complicated by the presence of two satellites, partially overlapping with the Ca $2p_{1/2}$ state. See text for details.

	Peak			
	$2p_{3/2}$	$2p_{1/2}$	Satellite 1	Satellite 2
Area (Parameter)	8127	4063	3745	3000
Area (Measured)	7027	3513	3745	3000
Position (Parameter)	346.77	350.47	350.68	354.5
Position (Measured)	346.51	350.21	350.68	354.4
FWHM (Parameter)	1.9	1.9	3.2	3.2
FWHM (Measured)	1.67	1.67	3.2	3.2
m (Gauss-Lorentz ratio - parameter)	1	1	0	0
a (Asymmetry - parameter)	1.82	1.82	0	0
b (Asymmetry shift - parameter)	0	0	0	0
Asymmetry: $\mathbf{1-\frac{FWHM_{right}}{FWHM_{left}}}$	0.46	0.46	0	0

Table 4. Numerical parameters of the least-squares fit of the 2p spectrum of Ca deposited onto rr-P3HT at 130 K.

The result of the least-squares fit crucially depends on the shape of the inelastic background which is subtracted from XPS spectra before fitting. Since such a procedure was not possible for the sample kept at 300 K in an unambiguous way, we will not further discuss the corresponding spectrum. In fitting the Ca 2p spectrum acquired from the sample kept at 130 K, the article of Leiro and Minni[132] was used to estimate the rough shape of a Shirley type signal background. Furthermore, the fact that the Ca $2p_{1/2}$ state strongly overlaps with satellites further complicates the analysis. However, according to Leiro and Minni[132] two major satellite lines should be located approximately 4 eV and 9 eV above the $2p_{3/2}$ peak. Under those constraints, it was possible to deconvolute the Ca 2p spectrum of the 130 K sample into a strongly asymmetric Ca 2p doublet (gray shaded in Figure 21) and two satellite lines. The results of the fitting procedure are listed in Table 4.

3.2.3 Pd nanoparticles and their interaction with ionic liquids [P7]

The article [P7] was published in close cooperation with the group of Prof. Dr. J. Libuda at the University of Erlangen-Nürnberg, and in particular with M.Sc. Marek Sobota. The excellent cooperation is gratefully acknowledged. The application of ionic liquids in advanced catalytic approaches such as SILP[55,56] and SCILL[58] requires a detailed knowledge on the interaction between the IL overlayer and the Pd nanoparticles. We examined in particular the chemical stability of thin layers of the room temperature ionic liquid [BMIM][Tf_2N] on the model catalyst surface Pd/Al_2O_3/NiAl(110) at 300 K and elevated temperatures. All measurements have been performed under ultrahigh vacuum conditions. The corresponding films have been prepared by physical vapor deposition.[60] Figure 22 shows a sketch of the investigated system. We will briefly review the key results, obtained by employing infrared adsorption spectroscopy (IRAS). [P7]

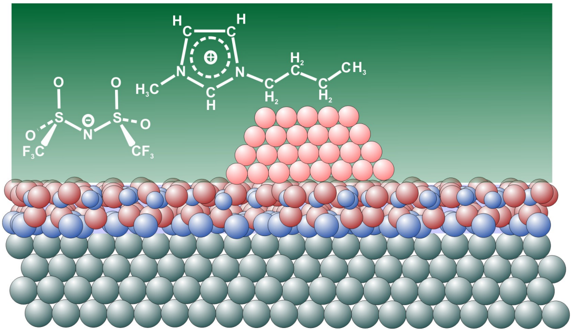

Figure 22. [BMIM][Tf_2N] adsorbed on the model catalyst Pd/Al_2O_3/NiAl(110); reprint from [P7] - Reproduced by permission of the PCCP Owner Societies.

(i) [BMIM][Tf_2N] adsorbs molecularly on the Pd nanoparticles as well as on the aluminium oxide support. The IRAS results suggest an interaction of the [Tf_2N] anion with the Pd nanoparticles mediated by the SO_2 groups. However, due to the low intensity of the corresponding signals it is not possible to comment on the bonding situation for the [BMIM] cation.

(ii) If carbon monoxide is used to probe the different adsorption sites on the Pd nanoparticles and their occupation as a function of the IL coverage, a displacement of CO from the majority of its adsorption sites on the Pd nanoparticles is evident.

(iii) In contrast to nanoparticle-free $Al_2O_3/NiAl(110)$ substrates,[133] a thermal desorption of the ionic liquid from the $Pd/Al_2O_3/NiAl(110)$ surface is not possible without severe decomposition.

At this point, photoelectron spectroscopy was employed to further elucidate the process of the molecular decomposition of the ionic liquid layer on the model catalyst surface.[P7] We will now briefly review the most significant results. To clarify the temperature stability of the ionic liquid layers, XP spectra were recorded at room temperature, 373 K, and 473 K. The room temperature spectra confirmed the IRAS results of a molecular adsorption of the ionic liquid; no indications for a degradation of the compound were present and the different intensity ratios were in line with the molecular stoichiometry of the sample. After heating to 373 K, first indications for molecular desorption of parts of the film became evident, however, without any indications for a degradation of the molecules. Further heating to 473 K led to a substantially different situation, as illustrated in Figure 23. After heating the sample to 473 K, a substantial mismatch between the photoelectron intensities of the different ionic liquid elements became evident. This finding, together with a significant modification of, e.g., the sulphur 2p core level, indicated a decomposition of the IL film upon heating. The XP core level spectra of the substrate species Al and Pd increased by a different amount; the Pd signal was significantly more attenuated then the Al signal. Accordingly, one can conclude that mostly the Pd nanoparticles were covered with the decomposition products of the IL. This is in line with the experimental finding that the ion liquid $[BMIM][Tf_2N]$ desorbs intact from pure $Al_2O_3/NiAl(110)$ substrates,[133] and the blocking of Pd-adsorption sites observed with IRAS. While the decomposition products are mainly comprised of carbon and nitrogen, the other elements, present in particular in the $[Tf_2N]$ anion, are residing on the surface

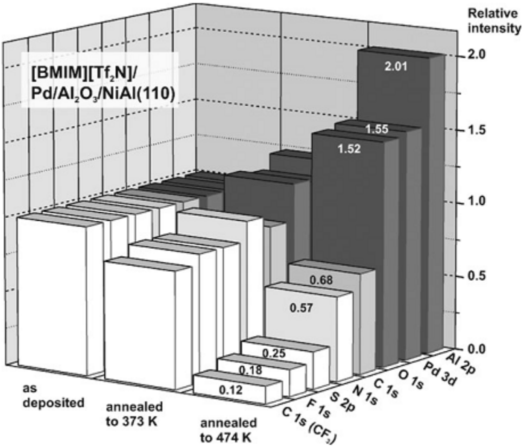

Figure 23. The evolution of a thin ionic liquid film on the Pd/Al/Ni substrate; reprint from [P7] - Reproduced by permission of the PCCP Owner Societies.

to a significantly smaller amount. A close examination of traces of sulphur (intensity reduced to 25%) and flourine (intensity reduction to 18%) suggests the formation of SF_x and / or SO_xF_y species on the surface. The predominant covering of the sample surface with decay products originating from the [BMIM] (compare Figure 23) cation can be rationalized in two ways. First, it appears likely that the [BMIM] cation is gradually dehydrogenated on the Pd nanoparticles, since dehydrogenation reactions are well known to occur on transition metals.[134] Second, the S, F, N, and O atoms, building up the anion, all have relatively high electronegativities, thus having a tendency to form small stable molecules such as N_2, NH_3, or SO_2; molecules which could easily leave the surface after their formation. While in the pristine films the interaction between the Pd clusters and the IL is mainly mediated by the [Tf_2N] anion, the molecular decay products mainly originate from the [BMIM] cation. However, a detailed analysis of the decomposition products could be subject to further investigations, for instance in further TPD experiments.

4 Summary

In this thesis, interfaces between metals and organic thin films have been characterized with photoelectron and ion-scattering spectroscopies. Two different classes of metal/organic interfaces were examined in detail. First, interfaces which can be mainly characterized by relatively weak coordinative interactions between substrate and adsorbate. Second, interfaces which are mostly determined, or even created, by chemical reactions between different adsorbates or between adsorbates and substrate.

Typical examples from the first class are metalated tetrapyrrole monolayers on Ag(111) and Au(111) single-crystal substrates. The scientific interest in those systems stems from the fact that modifications of interfacial properties by the adsorption of porphyrins or phthalocyanines have been utilized in fields such as catalysis, gas-sensing, and organic electronics. In this study, a focus was set to the interaction between iron and cobalt tetrapyrroles with Ag(111) or Au(111) substrates. Generally, the modification of those adsorbate molecules by a direct contact to the substrate was found to be most prominent for the central metal ion. A detailed examination of the corresponding photoelectron spectra revealed that the adsorbate-substrate interaction is associated with a charge transfer from the metallic substrate to the Fe(II) or Co(II) ions within the tetrapyrrole units. The examination of cobalt(II) phthalocyanine monolayers further led to the conclusion that the magnetic moment, as present in unperturbed CoPc molecules, is efficiently quenched by the contact to the Ag(111) surface and the associated charge transfer. Similar investigations on Au(111) substrates gave evidence for possible adsorption site effects, further complicating the adsorbate/substrate interaction. In contrast to the coupling between the central metal atoms and the silver or gold substrates, the interaction between the individual molecules within a monolayer is relatively weak. The van der Waals forces, responsible for the well ordered morphology of tetrapyrrole monolayers, provide only a limited mechanical stability of the corresponding films.

A possible route towards the fabrication of more robust adsorbate layers is a temperature-activated polymerization between adjacent adsorbate molecules. In particular halogen substituted compounds were found to be suitable for this kind of process. The interfaces obtained by this approach are mostly determined by the chemical process associated with the formation of the covalent adsorbate structure. In this thesis, the formation of two-dimensional structures of poly(*p*--phenylene- terephthalamide) (PPTA, trademark *Kevlar*) on Ag(111) was closely examined. The synthesis of those structures is feasible by the co-adsorption of the precursor molecules *p*-terephthaloylchloride (TPC) and *p*-phenylenediamine (PPD). It was demonstrated that the reaction mechanism on the Ag(111) surface is substantially different from the mechanism found in the corresponding process in solution. The Ag(111) surface does not only provide the geometrical boundary for the formation of the 2D covalent structures, but, moreover, actively participates in the reaction; after the adsorption of TPC molecules, a scission of the C-Cl bond, in particular at temperatures above 120 K, was evident. This reaction is directly related to the vicinity of the Ag(111) substrate. The resulting radical fragments appear stable and can act as reaction partners for the co-adsorbed PPD units. The chlorine atoms reside on the surface even at elevated temperatures (400 K).

A further system whose properties were also mostly determined by a chemical reaction between substrate and adsorbate was observed in form of the interface between calcium and the polymer poly(3--hexylthiophene) (rr-P3HT). In this case, the metal served as adsorbate (deposited via physical vapor deposition, PVD) while the polymer was used as a substrate. The properties of this technologically relevant interface are significantly determined by a chemical reaction between Ca atoms that diffused into the bulk polymer and the sulphur atoms in thiophene units. The formation of a reaction layer between the metallic calcium and the semiconducting polymer potentially has a negative influence to the performance of corresponding devices. It could be shown that a reduction of the temperature during the metal deposition (130 K) results in the formation of a significantly better, i.e. sharper, interface between calcium and the semiconducting thiophene polymer.

In contrast to the latter interface, which is mainly of importance in the field of organic electronics, in particular in the fabrication of organic solar cells, the following system is of interest in the field of catalysis. We examined the model catalyst Pd/Al_2O_3/NiAl(110) (where an adsorbate layer of Pd nanoparticles provides the catalytic activity) covered with a thin film of the room temperature ionic liquid 1-butyl-3-methylimidazolium bis(trifluoromethylsulfonyl)imide, [BMIM][Tf_2N]. Such interfaces play a decisive role within novel concepts in catalysis, as for instance SCILL (Solid Catalyst with Ionic Liquid Layer) and SILP (Supported Ionic Liquid Phase); there, the ionic liquid layer acts as a semipermeable membrane or selective solvent within a catalytic process. For those applications, it is of primary importance that the individual components, such as the ionic liquid, are inert under reaction conditions. At room temperature and 100 °C, [BMIM][Tf_2N] showed no indications for decomposition processes. However, at 200 °C, the catalyst surface is mostly comprised of decomposition products of the ionic liquid, efficiently blocking the catalytically active sites on the Pd nanoparticles. Similar experiments on the pristine Al_2O_3/NiAl(110) without the Pd nanoparticles showed a complete desorption of the ionic liquid film upon heating to sufficiently high temperatures. Hence, it can be concluded that the catalytically active Pd nanoparticles also lead to the decomposition of ionic liquid films at elevated temperatures; a result that should be kept in mind during the design of IL-based catalyst concepts.

Zusammenfassung

In dieser Arbeit wurden verschiedene Grenzflächen zwischen Metallen und organischen Dünnschichten mit Hilfe von Photoelektronen- und Ionenstreuspektroskopie charakterisiert. Dabei lag der Fokus zum einen auf Grenzschichten deren Eigenschaften überwiegend durch vergleichsweise schwache, koordinative Wechselwirkungen bestimmt werden und zweitens, Grenzflächen deren Eigenschaften durch chemische Reaktionen definiert werden, die sowohl Adsorbat als auch Substrat signifikant verändern.

Typische Vertreter der erstgenannten Kategorie sind metallierte Tetrapyrrol-Monolagen auf Ag(111) oder Au(111) Einkristallen, wobei erwähnenswert ist, dass Oberflächenmodifikationen durch die Adsorption von Porphyrinen oder Phthalocyaninen bereits Anwendung in Bereichen wie Katalyse, Gas-Sensorik oder organischer Elektronik fanden. In dieser Studie wurde insbesondere die Wechselwirkung zwischen Eisen- und Cobalt-Tetrapyrrolen und den genannten Oberflächen untersucht. Dabei zeigte sich, dass sich die Modifikation der Moleküle in direktem Kontakt zum Substrat im Allgemeinen auf das zentrale Metallatom beschränkt. Aus einer genauen Untersuchung und Analyse der entsprechenden Photoelektronenspektren konnte gefolgert werden, dass die Substrat-Adsorbat Wechselwirkung mit einem Ladungstransfer vom metallischen Substrat hin zu den zentralen Fe(II) oder Co(II) Ionen der adsorbierten Tetrapyrrole verbunden ist. Insbesondere zeigte sich bei Cobalt(II)phthalocyanin-Schichten, dass das magnetische Moment der einzelnen CoPc Moleküle durch den direkten Kontakt zu einer Ag(111) Oberfläche und den damit verbundenen Ladungstransfer komplett unterdrückt wird. Auf Au(111) Oberflächen wurden zudem Hinweise für eine Adsorptionsplatzabhängigkeit der oben geschilderten Effekte gefunden.

Im Gegensatz zu der Kopplung zwischen den zentralen Metallionen und den Silber- bzw. Goldsubstraten ist die Wechselwirkung zwischen einzelnen Molekülen in letzteren Systemen relativ schwach ausgeprägt und führt lediglich zu einer durch van-der-Waals Kräfte vermittelten Selbstordnung der Adsorbatlage. Betrachtet man solche Lagen unter mechanischen Gesichtspunkten, sind solche Schichten nur von begrenzter Robustheit. Ein möglicher Weg der Erzeugung

mechanisch widerstandfähigerer Adsorbatstrukturen besteht in einer temperaturinduzierten Polymerisationsreaktion zwischen den Adsorbatmolekülen. Für diese Art von Reaktion haben sich vor allem halogensubstituierte Kohlenwasserstoffe als brauchbar erwiesen. Die Eigenschaften derartig erzeugter Grenzflächen werden dementsprechend hauptsächlich durch die chemischen Prozesse definiert, die mit der kovalenten Verknüpfung der Adsorbatmoleküle einhergehen. Im Rahmen dieser Arbeit wurde die Synthese von zweidimensionalen Poly(*p*-Phenylenterephthalamid) Strukturen (PPTA, besser bekannt unter dem Handelsnamen *Kevlar*) auf Ag(111) näher beleuchtet. Die Synthese dieser Strukturen kann durch eine Koadsorption der Moleküle *p*-Terephthaloylcholrid (TPC) und *p*-Phenylendiamin (PPD) erreicht werden. Insbesondere konnte gezeigt werden, dass sich der Reaktionsmechanismus auf der Ag(111) Oberfläche signifikant vom entsprechenden Reaktionsmechanismus in Lösung unterscheidet. Die Ag(111) Oberfläche definiert nicht nur passiv den geometrischen Rahmen für die Ausbildung der zweidimensionalen PPTA Strukturen, sondern ist auch selbst wesentlich am Reaktionsverlauf beteiligt; nach der Adsorption von TPC spaltet sich oberhalb von Temperaturen von 120 K das Chloratom vom Molekül ab. Dieser Zerfall ist unmittelbar durch die Silberoberfläche induziert. Das entstehende radikalische Molekülfragment zerfällt nicht weiter und steht als Reaktionspartner für die Polymerisation mit PPD zur Verfügung. Das Chloratom verbleibt auch bei höheren Temperaturen (400 K) auf der Ag(111) Oberfläche.

Ein ähnliches System, dessen Eigenschaften ebenfalls weitestgehend durch eine chemische Reaktion zwischen Substrat und Adsorbat festgelegt sind, lag in Form der Grenzfläche zwischen metallischem Calcium und dem Polymer Poly(3-Hexylthiophen) (rr-P3HT) vor. In diesem Fall diente das organische Material als Substrat, während das Metall durch Aufdampfen auf die Probe aufgebracht wurde. Die Eigenschaften dieser technisch relevanten Grenzfläche sind signifikant durch eine Reaktion von diffundierten Ca-Atomen mit Schwefel aus den Thiophengruppen im Polymer bestimmt, wobei sich die Bildung einer Reaktionsschicht zwischen dem metallischen Calcium und dem halbleitenden Polymersubstrat sich potentiell negativ auf die Eigenschaften elektronischer Bauteile auswirkt, die einen solchen Metall-Halbleiter Kontakt enthalten. Im Rahmen dieser Arbeit konnte gezeigt werden, dass eine Verringerung der Temperatur bei der Ca-Abscheidung auf 130 K zu einer weitaus besser definierten Grenzfläche zwischen metallischem Calcium und dem Trägerpolymer führt.

Im Gegensatz zu den bisher untersuchten Grenzschichten ist das zuletzt diskutierte Substrat-Adsorbat System im Bereich der heterogenen Katalyse angesiedelt. Gegenstand dieser Experimente war die Grenzfläche zwischen dem Modellkatalysator Pd/ Al_2O_3/NiAl(110) (in diesem Fall stellen Pd-Nanopartikel auf dem Aluminiumsubstrat die katalytisch aktiven Zentren dar) und einer dünnen Schicht der ionischen Flüssigkeit 1-Butyl-3-methylimidazolium-bis(trifluoromethylsulfonyl)imid, abgekürzt $[BMIM][Tf_2N]$. Solche Grenzflächen spielen eine entscheidende Rolle in neueren Katalysekonzepten, wie zum Beispiel SCILL (Solid Catalyst with Ionic Liquid Layer) und SILP (Supported Ionic Liquid Phase), bei denen die ionische Flüssigkeit effektiv wie eine selektive Membran oder ein hochselektives Lösungsmittel für den katalytischen Prozess wirken soll. Für derartige Anwendungen spielt die Inertheit der beteiligten Komponenten eine entscheidende Rolle. Bei Raumtemperatur und bei Temperaturen von bis zu 100°C zeigte die ionische Flüssigkeit $[BMIM][Tf_2N]$ keinerlei Anzeichen für unerwünschte Reaktionen mit dem Pd-Modellkatalysator. Die Situation änderte sich signifikant bei weiterer Temperaturerhöhung. Bei Temperaturen von 200°C besteht die Grenzfläche weitestgehend nur noch aus Zerfallsfragmenten der ionischen Flüssigkeit, die darüber hinaus effektiv die katalytisch aktiven Zentren an den Pd-Nanopartikeln passivieren. Entsprechende Experimente auf der Modellkatalysatoroberfläche ohne die Pd-Nanopartikel ergaben hingegen eine vollständige Desorption der ionischen Flüssigkeit, ohne Hinweise auf irgendwelche molekularen Zerfallsreaktionen zu liefern. Daraus folgt, dass die katalytisch aktiven Nanopartikel bei höheren Temperaturen ebenfalls die Zersetzung der umgebenden ionischen Flüssigkeit herbeiführen; dieses Ergebnis sollte bei der Entwicklung von IL-basierten Katalysatorkonzepten berücksichtigt werden.

5 Acknowledgement

At this point, the author must not miss to express his gratitude to several persons from the Lehrstuhl für Physikalische Chemie II.

Professor Hans-Peter Steinrück For providing an excellent environment for scientific work as well as stimulating and constructive discussions.

Professor J. Michael Gottfried His kind guidance and advice never failed to improve things.

Dr. Yun Bai For instructing the author during his first steps in the laboratory.

Mr. Hans-Peter Bäumler and Mr. Bernd Kress For their profound expertise and high motivation when a technical problem had to be solved.

All members of the mechanical workshop For their excellent work.

All members of the institute It was a pleasure to work with all of you.

6 Bibliography

References

[1] Henzler, M.; Göpel, W. *Oberflächenphysik des Festkörpers*; Teubner B.G. GmbH, 1994.

[2] Burroughes, J. H.; Bradley, D. D. C.; Brown, A. R.; Marks, R. N.; Mackay, K.; Friend, R. H.; Burns, P. L.; Holmes, A. B. *Nature* **1990**, *347*, 539 – 541.

[3] Schwartz, G.; Fehse, K.; Pfeiffer, M.; Walzer, K.; Leo, K. *Appl. Phys. Lett.* **2006**, *89*, 083509.

[4] Kelley, T. W.; Baude, P. F.; Gerlach, C.; Ender, D. E.; Muyres, D.; Haase, M. A.; Vogel, D. E.; Theiss, S. D. *Chemistry of Materials* **2004**, *16*, 4413–4422.

[5] Schmidt-Mende, L.; Fechtenkötter, A.; Müllen, K.; Moons, E.; Friend, R. H.; MacKenzie, J. D. *Science* **2001**, *293*, 1119–1122.

[6] Peumans, P.; Uchida, S.; Forrest, S. R. *Nature* **2003**, *425*, 158 – 162.

[7] Ma, W.; Yang, C.; Gong, X.; Lee, K.; Heeger, A. J. *Advanced Functional Materials* **2005**, *15*, 1617–1622.

[8] Mansuy, D.; Battioni, P. In *The porphyrin handbook*; Kadish, K. M., Smith, K. M., Guilard, R., Eds.; Academic Press, San Diego, 2000; Vol. 4; Chapter Diversity of reactions catalyzed by heme-thiolate proteins, p 1.

[9] Poulos, T. L. In *The porphyrin handbook*; Kadish, K. M., Smith, K. M., Guilard, R., Eds.; Academic Press, San Diego, 2000; Vol. 4; Chapter Peroxidase and cytochrome P450 structures, p 189.

[10] Kadish, K. M., Smith, K. M., Guilard, R., Eds. *The porphyrin handbook: Chlorophylls and Bilins: Biosynthesis, synthesis and degradation*; Academic Press, San Diego, 2003; Vol. 13.

[11] Kurreck, J.; Niethammer, D.; Kurreck, H. *Chemie in unserer Zeit* **1999**, *33(2)*, 72 – 83.

[12] Harriman, A.; Sauvage, J.-P. *Chem. Soc. Rev.* **1996**, *25*, 41 – 48.

[13] Zeller, M. V.; Hayes, R. G. *J. Am. Chem. Soc.* **1973**, *95(12)*, 3855 – 3860.

[14] Karweik, D.; Winograd, N.; Davis, K. M., D. G. Kadish *J. Am. Chem. Soc.* **1974**, *96(2)*, 591 – 592.

[15] Frost, D. C.; McDowell, C. A.; Woosley, I. S. *Mol. Phys.* **1974**, *27(6)*, 1473 – 1489.

[16] Borod'ko, Y. G.; Vetchinkin, S. I.; Zimon, S. L.; Ivleva, I. N.; Shul'ga, Y. M. *Chem. Phys. Lett.* **1976**, *42(2)*, 264 – 267.

[17] Uchida, K.; Soma, M.; Onishi, T.; Tamaru, K. *Inorg. Chim. Acta* **1978**, *26*, L3 – L4.

[18] Quedraogo, G. V.; Benlian, D.; Porte, L. *J. Chem. Phys.* **1980**, *73(2)*, 642 – 647.

[19] Kadish, K. M.; Bottomley, L. A.; Brace, J. G.; Winograd, N. *J. Am. Chem. Soc.* **1980**, *102(13)*, 4341 – 4344.

[20] Nishimura, N.; Ooi, M.; Shimazu, K.; Fujii, H.; Uosaki, K. *J. Electroanal. Chem.* **1999**, *473*, 75 – 84.

[21] Love, J. C.; Estroff, L. A.; Kriebel, J. K.; Nuzzo, R. G.; Whitesides, G. M. *Chem. Rev.* **2005**, *105*, 1103 – 1169.

[22] Hanzlikova, J.; Prochazka, M.; Stepanek, J.; Bok, J.; Baumruk, V.; Anzenbacher, P. *J. Raman Spectrosc.* **29**, *1998*, 575.

[23] Tsukahara, S.; Suzuki, N. *Inorg. Chim. Acta* **1996**, *245*, 105.

[24] Gottfried, J. M.; Flechtner, K.; Kretschmann, A.; Lukasczyk, T.; Steinrück, H.-P. *J. Am. Chem. Soc.* **2006**, *128*, 5644 – 5645.

[25] Shubina, T. E.; Marbach, H.; Flechtner, K.; Kretschmann, A.; Jux, N.; Buchner, F.; Steinrück, H.-P.; Clark, T.; Gottfried, J. M. *J. Am. Chem. Soc.* **2007**, *129*, 9476 – 9483.

[26] Mochida, I.; Suetsugu, K.; Fujitsu, H.; Takeshita, K. *J. Phys. Chem.* **1983**, *87*, 1524 – 1529.

[27] Kalyanasundaram, K.; Grätzel, M. *Helv. Chim. Acta* **1980**, *63(2)*, 478 – 485.

[28] Guillaud, G.; Simon, J.; Germain, J. P. *Coord. Chem. Rev.* **1998**, *178 - 180*, 1433 – 1484.

[29] Kwong, C. Y.; Djuršić, A. B.; Lam, L. S. M.; Chan, W. K. *Proceedings of SPIE: Organic Photovoltaics III* **2003**, *4801*, 7 – 14.

[30] Takulapalli, B. R.; Laws, G. M.; Liddell, P. A.; Andreasson, J.; Erno, Z.; Gust, D.; Thornton, T. J. *J. Am. Chem. Soc.* **2008**, *130*, 2226 – 2233.

[31] Flechtner, K.; Kretschmann, A.; Bradshaw, L. R.; Walz, M.-M.; Steinrück, H.-P.; Gottfried, J. M. *J. Phys. Chem. C: Letters* **2007**, *111*, 5821 – 5824.

[32] Flechtner, K.; Kretschmann, A.; Steinrück, H.-P.; Gottfried, J. M. *J. Am. Chem. Soc.* **2007**, *129*, 12110 – 12111.

[33] Lukasczyk, T.; Flechtner, K.; Merte, L. R.; Jux, N.; Maier, F.; Gottfried, J. M.; Steinrück, H.-P. *J. Phys. Chem. C* **2007**, *111*, 3090 – 3098.

[34] Buchner, F.; Flechtner, K.; Bai, Y.; Zillner, E.; Kellner, I.; Steinrück, H.-P.; Marbach, H.; Gottfried, J. M. *J. Phys. Chem. C* **2008**, *112*, 15458 – 15465.

[35] Bai, Y.; Buchner, F.; Wendahl, M. T.; Kellner, I.; Bayer, A.; Steinrück, H.-P.; Marbach, H.; Gottfried, J. M. *J. Phys. Chem. C* **2008**, *112*, 6087 – 6092.

[36] Bai, Y.; Buchner, F.; Kellner, I.; Schmid, M.; Vollnhals, F.; Steinrück, H.-P.; Marbach, H.; Gottfried, J. M. *New J. Phys.* **2009**, *11*, 125004.

[37] Gottfried, J. M.; Marbach, H. *Z. Phys. Chem.* **2009**, *223*, 53 – 74.

[38] Grill, L.; Dyer, M.; Lafferentz, L.; Persson, M.; Peters, M. V.; Hecht, S. *Nat. Nanotechnol.* **2007**, *2*, 687 – 691.

[39] Lipton-Duffin, J. A.; Ivasenko, O.; Perepichka, D. F.; Rosei, F. *Small* **2009**, *5*, 592–597.

[40] Gutzler, R.; Walch, H.; Eder, G.; Kloft, S.; Heckl, W. M.; Lackinger, M. *Chem. Commun.* **2009**, *29*, 4456–4458.

[41] Bieri, M.; Nguyen, M.-T.; Groöning, O.; Cai, J.; Treier, M.; Ait-Mansour, K.; Ruffieux, P.; Pignedoli, C. A.; Passerone, D.; Kastler, M.; Müllen, K.; Fasel, R. *J. Am. Chem. Soc.* **2010**, *132*, 16669–16676.

[42] Schmitz, C. H.; Ikonomov, J.; Sokolowski, M. *J. Phys. Chem. C: Letters* **2009**, *113*, 11984 – 11987.

[43] Bender, M. L. *Chem. Rev.* **1960**, *60*, 53 – 113.

[44] Zhou, X.-L.; Solymosi, F.; Blass, P.; Cannon, K.; White, J. *Surf. Sci.* **1989**, *219*, 294 – 316.

[45] Szulczewski, G. J.; White, J. M. *Surf. Sci.* **1998**, *399*, 305 – 315.

[46] Friend, R. H.; Gymer, A. B., R. W. Holmes; Burroughes, J. H.; Marks, R. N.; Taliani, C.; Bradley, D. D. C.; Dos Santos, D. A.; Bredas, J. L.; Loglund, M.; Salaneck, W. R. *Nature* **1999**, *397*, 121 – 128.

[47] Fahlman, W.; Salaneck, W. R. *Surf. Sci.* **2002**, *500(1 - 3)*, 904 – 922.

[48] Cheng, H.-L.; Lin, J.-W.; Jang, M.-F.; Wu, F.-C.; Chou, W.-Y.; Chang, M.-H.; Chao, C.-H. *Macromolecules* **2009**, *42*, 8251 – 8259.

[49] Coakley, K. M.; McGehee, M. D. *Chem. Mater.* **2004**, *16*, 4533 – 4542.

[50] Hugger, S.; Thomann, R.; Heinzel, T.; Thurn-Albrecht, T. *Colloid Polym. Sci.* **2004**, *282*, 932 – 938.

[51] Zhu, J.; Bebensee, F.; Hieringer, W.; Zhao, W.; Baricuatro, J. H.; Farmer, J. A.; Bai, Y.; Steinrück, H.-P.; Gottfried, J. M.; Campbell, C. T. *J. Am. Chem. Soc.* **2009**, *131*, 13498 – 13507.

[52] Wasserscheid, P.; Welton, T. *Ionic Liquids in Synthesis*; Willey-VCH,Weinheim, 2007.

[53] Brennecke, J. F.; Rogers, R. D.; Seddon, K. R. *Ionic Liquids IV - Not just solvents anymore*; Oxford University Press, 2007.

[54] Plechkova, N. V.; Seddon, K. R. *Chem. Soc. Rev.* **2008**, *37*, 123 – 150.

[55] Riisager, A.; Wasserscheid, P.; van Hal, R.; Fehrmann, R. *J. Catal.* **2003**, *219*, 452 –455.

[56] Riisager, A.; Eriksen, K. M.; Wasserscheid, P.; Fehrmann, R. *Catal. Lett.* **2003**, *90*, 149 –153.

[57] Mehnert, C. P.; Cook, R. A.; Dispenziere, N. C.; Afeworki, M. *J. Am. Chem. Soc.* **2002**, *124*, 12932 – 12933.

[58] Kernchen, U.; Etzold, B.; Korth, W.; Jess, A. *Chem. Eng. Technol.* **2007**, *30*, 985 – 994.

[59] Walden, P. *Bull. Accad. Impér. Sci. St. Pétersbourg* **1914**, *8*, 405 – 422.

[60] Cremer, T.; Killian, M.; Gottfried, J. M.; Paape, N.; Wasserscheid, P.; Maier, F.; Steinrück, H.-P. *Chem. Phys. Chem.* **2008**, *9*, 2185.

[61] Kolbeck, C.; Cremer, T.; Lovelock, K. R. J.; Paape, N.; Schulz, P. S.; Wasserscheid, P.; Maier, F.; Steinrück, H.-P. *J. Phys. Chem. B* **2009**, *113*, 8682.

[62] Lovelock, K. R. J.; Kolbeck, C.; Cremer, T.; Paape, N.; Schulz, P. S.; Wasserscheid, P.; Maier, F.; Steinrück, H.-P. *J. Phys. Chem. B* **2009**, *113*, 2854.

[63] Steinrück, H.-P. *Surf. Sci.* **2010**, *604*, 481 – 484.

[64] Steinrück, H.-P.; Libuda, J.; Wasserscheid, P.; Cremer, T.; Kolbeck, C.; Laurin, M.; Maier, F.; Sobota, M.; Schulz, P. S.; Stark, M. *Adv. Mater.* **2011**, *23*, 2571 – 2587.

[65] Bäumer, M.; Freund, H.-J. *Prog. Surf. Sci.* **1999**, *61*, 127.

[66] Libuda, J.; Meusel, I.; Hoffmann, J.; Hartmann, J.; Piccolo, L.; Henry, C. R.; Freund, H.-J. *J. Chem. Phys.* **2001**, *114*, 4669.

[67] Freund, H.-J. *Catal. Today* **2006**, *117*, 6 – 14.

[68] Rupprechter, G. *Catal. Today* **2007**, *126*, 3 – 17.

[69] Shockley, W. *Phys. Rev.* **1939**, *56*, 317 – 323.

[70] Shirley, D. A. *Phys. Rev. B* **1972**, *5*, 4709.

[71] Tougaard, S. *Surf. Sci.* **1989**, *216*, 343.

[72] Hüfner, S. In *Photoelectron Spectroscopy*; Cardona, M., Ed.; Springer, 1996.

[73] Einstein, A. *Ann. Physik* **1905**, *322(6)*[h], 132.

[74] Wien, W. *Ann. Physik* **1894**, *288(5)*, 132.

[75] Slater, J. C. *Quantum Theory of Atomic Structure*; McGraw-Hill, 1960; Vol. 1.

---

[h] Counting the volumes from the first published edition 1799. Alternative counting: 4th series, Volume 17, No. 6

[76] Wagner, C. D., Riggs, W. M., Davis, L. E., Moulder, J. F., Mullenberg, G. E., Eds. *Handbook of X-ray Photoelectron Spectroscopy*; Perkin-Elmer, USA, 1992.

[77] Pease, D. M. *Phys. Rev. B* **1991**, *44(13)*, 6708 – 6714.

[78] Fuggle, J. C.; Alvarado, S. F. *Phys. Rev. A* **1980**, *22(4)*, 1615 – 1624.

[79] Van der Heide, P. A. W. *J. Elec. Spec. and Rel. Phen.* **2008**, *164*, 8 – 18.

[80] Kowalczyk, S. P.; Ley, L.; McFeely, F. R.; Shirley, D. A. *Phys. Rev. B* **1975**, *11(4)*, 1721 – 1727.

[81] Hedman, J.; Heden, P.-F.; Nordling, C.; Siegbahn, K. *Phys. Lett. A* **1969**, *29*, 178.

[82] Fadley, C. S.; Shirley, D. A. *Phys. Rev. A* **1970**, *2(4)*, 1109 – 1120.

[83] Wertheim, G. K.; Hüfner, S.; Guggenheim, H. J. *Phys. Rev. B* **1973**, *7(1)*, 556.

[84] Bagus, P. S.; Freeman, A. J.; Sasaki, F. *Phys. Rev. Lett.* **1973**, *30*, 850 – 853.

[85] Gupta, R. P.; Sen, S. K. *Phys. Rev. B* **1974**, *10(1)*, 71 – 77.

[86] Gupta, R. P.; Sen, S. K. *Phys. Rev. B* **1975**, *12(1)*, 15 – 19.

[87] McIntyre, N.; Cook, M. G. *Anal. Chem.* **1975**, *47(13)*, 2208 – 2213.

[88] McIntyre, N.; Zetaruk, D. G. *Anal. Chem.* **1977**, *49(11)*, 1521 – 1529.

[89] Grosvenor, A. P.; Kobe, B. A.; Biesinger, M. C.; McIntyre, N. *Surf. Interface Anal.* **2004**, *36*, 1564 – 1574.

[90] Frost, D. C.; McDowell, C. A.; Woosley, I. S. *Chem. Phys. Lett.* **1972**, *17(3)*, 320 – 323.

[91] Ivanova, T.; Naumkin, A.; Sidorov, A.; Eremenko, I.; Kiskin, M. *J. Elec. Spec. and Rel. Phenom.* **2007**, *156 - 158*, 200 – 203.

[92] Briggs, D.; Gibbson, V. A. *Chem. Phys. Lett.* **1974**, *25(4)*, 493 – 496.

[93] Nefedov, V. I. *Izv. Nats. Akad. Nauk. Resp., Ser. Fiz.* **1964**, *28*, 816.

[94] Kittel, C. *Introduction to Solid State Physics*, 7th ed.; Wiley - New York, 1996.

[95] Lamont, C. L. A. *Langmuir* **1999**, *15*, 2037.

[96] Seah, M. P.; Dench, W. A. *Surf. Interface Anal.* **1979**, *1(1)*, 2 – 11.

[97] Penn, D. R. *Phys. Rev. B* **1976**, *13(12)*, 5248 – 5254.

[98] Grasserbauer, M.; Dudek, J.; Ebel, M. F. *Angewandte Oberflächenanalyse*; Springer-Verlag, 1986.

[99] Wagner, C. D. *J. Electron Spectroc. Relat. Phenom.* **1983**, *32*, 99 – 102.

[100] Ward, R. J.; Wood, B. J. *Surf. Interface Anal.* **1992**, *18*, 679 – 684.

[101] Doniach, S.; Sunujic, M. *J. Phys. C.: Solid State Phys.* **1970**, *3*, 285.

[102] Gelius, U.; Svensson, S.; Siegbahn, H.; Basilier, E.; Faxälv, Å.; Siegbahn, K. *Chem. Phys. Lett.* **1974**, *28*, 1 – 7.

[103] Armstrong, B. H. *J. Quant. Spectrosc. Radiat. Trans.* **1967**, *7*, 61 – 88.

[104] Sherwood, P. M. A. In *Practical Surface Analysis*, 2nd ed.; Briggs, D., Seah, M. P., Eds.; John Willey & Sons, 1990; Vol. 1.

[105] Hesse, R.; Streubel, P.; Szargan, R. *Surf. Interf. Anal.* **2007**, *39*, 381.

[106] Wertheim, G. K.; Butler, M. A.; West, K. W.; Buchanan, D. N. E. *Rev. Sci. Instrum.* **1974**, *45(11)*, 1369.

[107] Leiro, J. A.; Minni, E.; Suoninen, E. *J. Phys. F: Met. Phys.* **1983**, *13*, 215 – 221.

[108] Knöpfel, N.; Olbricht, T.; Schweig, A. *Chemie in unserer Zeit* **1971**, *5*, 65 – 77.

[109] Steinrück, H.-P.; Fuhrmann, T.; Papp, C.; Tränkenschuh, B.; Denecke, R. *J. Chem. Phys.* **2006**, *125*, 204706.

[110] Stancik, A. L.; Brauns, E. B. *Vibrational Spec.* **2008**, *47*, 66.

[111] Kibis, L. S.; Titkov, A. I.; Stadnichenko, A. I.; Koscheev, S. V.; Boronin, A. I. *Appl. Surf. Sci.* **2009**, *255*, 9248 – 9254.

[112] Briggs, D., Seah, M. P., Eds. *Practical Surface Analysis*, 2nd ed.; John Willey & Sons, 1990; Vol. 1.

[113] Gelius, U.; Wannberg, B.; Baltzer, P.; Fellner-Feldegg, H.; Carlsson, G.; Johansson, C.-G.; Larsson, J.; Münger, O.; Vegerfors, G. *J. Elec. Spec. Rel. Phen.* **1990**, *52*, 747 – 785.

[114] Roy, D. *Rep. Prog. Phys.* **1990**, *53*, 1621.

[115] Grosser, J. *Einführung in die Teilchenoptik*; Teubner B.G. GmbH, 1983.

[116] Hecht, E. *Optik*, 3rd ed.; Oldenbourg, 2001.

[117] Zangwill, A. *Physics at Surfaces*; Cambridge University Press, 1996.

[118] Thompson, D. *Am. J. Phys.* **1995**, *64*, 333 – 334.

[119] Omar, A. M. In *Elementary Solid State Physics*; Lazarus, D., Ed.; Addison Wesley, 1975.

[120] Niehus, H.; Spitzl, R. *Surf. Interf. Anal.* **1991**, *17*, 287.

[121] Niehus, H.; Heiland, W.; Taglauer, E. *Surf. Sci. Rep.* **1993**, *17*, 213.

[122] Baran, J. D.; Larsson, J. A.; Woolley, R. A. J.; Cong, Y.; Moriarty, P. J.; Cafolla, A. A.; Schulte, K.; Dhanak, V. R. *Phys. Rev. B* **2010**, *81*, 075413.

[123] Cheng, Z. H.; Gao, L.; Deng, Z. T.; Jiang, N.; Liu, Q.; Shi, D. X.; Du, S. X.; Guo, H. M.; Gao, H.-J. *J. Phys. Chem. C* **2007**, *111*, 9240 – 9244.

[124] Cheng, Z. H.; Gao, L.; Deng, Z. T.; Liu, Q.; Jiang, N.; Lin, X.; He, X. B.; Du, S. X.; Gao, H.-J. *J. Phys. Chem. C* **2007**, *111*, 2656 –2660.

[125] Umbach, E.; Seidel, C.; Taborski, J.; Soukopp, A. *Phys. Stat. Sol.* **1995**, *192*, 389.

[126] Isvoranu, C.; Wang, B.; Schulte, K.; Ataman, E.; Knudsen, J.; Andersen, J. N.; Bocquet, M.-L.; Schnadt, J. *J. Phys.: Condens. Matter* **2010**, *22*, 472002.

[127] Isvoranu, C.; Wang, B.; Ataman, E.; Schulte, K.; Knudsen, J.; Andersen, J. N.; Bocquet, M.-L.; Schnadt, J. *J. Chem. Phys* **2011**, *134*, 114710.

[128] Auwärter, W.; Seufert, K.; Klappenberger, F.; Reichert, J.; Weber-Bargioni, A.; Verdini, A.; Cvetko, D.; Dell'Angela, M.; Floreano, L.; Cossaro, A.; Bavdek, G.; Morgante, A.; Seitsonen, A. P.; Barth, J. V. *Phys. Rev. B* **2010**, *81*, 245403.

[129] Gao, L.; Ji, W.; Hu, Y. B.; H., C. Z.; Deng, Z. T.; Liu, Q.; Jiang, N.; Lin, X.; Guo, W.; Du, S. X.; Hofer, W. A.; Xie, X. C.; Gao, H.-J. *Phys. Rev. Lett.* **2007**, *99*, 106402.

[130] Bebensee, F.; Zhu, J.; Baricuatro, J. H.; Farmer, J. A.; Bai, Y.; Steinrück, H.-P.; Campbell, C. T.; Gottfried, J. M. *Langmuir* **2010**, *26*, 9632 – 9639.

[131] Ettedgui, E.; Razafitrimo, H.; Park, K. T.; Gao, Y.; Hsieh, B. R. *Surf. Interf. Anal.* **1995**, *23*, 89 – 98.

[132] Leiro, J. A.; Minni, E. E. *Phys. Rev. B* **1985**, *31*, 8248 – 8251.

[133] Sobota, M.; Nikiforidis, I.; Hieringer, W.; Paape, N.; Happel, M.; Steinrück, A., H.-P. Görling; Wasserscheid, P.; Laurin, M.; Libuda, J. *Langmuir* **2010**, *26*, 7199 – 7207.

[134] Ahmed, S.; Aitani, A.; Rahman, F.; Al-Dawood, A.; Al-Muhaish, F. *Applied Catalysis A: General* **2009**, *359*, 1 – 24.

7 Appendix: [P1] – [P7]

[P1] *The Electronic Structure of Cobalt(II) Phthalocyanine Adsorbed on Ag(111)*
Martin Schmid, Andre Kaftan, Hans-Peter Steinrück, J. Michael Gottfried
Surface Science, **2012**, accepted for publication

[P2] *Interfacial Interactions of Iron(II) Tetrapyrrole Complexes on Au(111)*
Martin Schmid, Johannes Zirzlmeier, Hans-Peter Steinrück, J. Michael Gottfried
J. Phys. Chem. C, **2011**, 115, 17028 - 17035

[P3] *Interfacial coordination interactions studied on cobalt octaethylporphyrin and cobalt tetraphenylporphyrin monolayers on Au(111)*
Yun Bai, Michael Sekita, **Martin Schmid**, Thomas Bischof, Hans-Peter Steinrück, J. Michael Gottfried
Phys. Chem. Chem. Phys., **2010**, 12, 4336 - 4344

[P4] *Adsorption and Reaction of Terephthaloyl Chloride on Ag(111): X-ray Photoelectron Spectroscopy and Density Functional Theory Investigations*
Martin Schmid, Wolfgang Hieringer, Christoph H. Schmitz, Hans-Peter Steinrück, Moritz Sokolowski, J. Michael Gottfried
J. Phys. Chem. C, **2011**, 115, 14869 - 14875

[P5] *Surface Polymerization of Poly(p-phenylene-terephthalamide) on Ag(111) Investigated by X-ray Photoelectron Spectroscopy and Scanning Tunneling Microscopy*
Christoph H. Schmitz, **Martin Schmid**, Stefan Gärtner, Hans-Peter Steinrück, J. Michael Gottfried, Moritz Sokolowski
J. Phys. Chem. C, **2011**, 115, 18186 - 18194

[P6] *Toward Well-Defined Metal-Polymer Interfaces: Temperature-Controlled Suppression of Subsurface Diffusion and Reaction at the Calcium/Poly(3-Hexylthiophene) Interface*
Fabian Bebensee, **Martin Schmid**, Hans-Peter Steinrück, Charles T. Campbell, J. Michael Gottfried
J. Am. Chem. Soc., **2010**, 132, 12163 - 12165

[P7] *Ionic liquid based model catalysis: interaction of* [BMIM][Tf_2N] *with Pd nanoparticles supported on an ordered alumina film*
Marek Sobota, **Martin Schmid**, Markus Happel, Max Amende, Florian Maier, Hans-Peter Steinrück, Natalia Paape, Peter Wasserscheid, Mathias Laurin, J. Michael Gottfried, Jörg Libuda
Phys. Chem. Chem. Phys., **2010**, 12, 10610 - 10621